Journal of Volcanology and Geothermal Research 297 (2015) 52–68

Contents lists available at ScienceDirect

Journal of Volcanology and Geothermal Research

journal homepage: www.elsevier.com/locate/jvolgeores

Permeability and porosity relationships of edifice-forming andesites: A combined field and laboratory study

Jamie Farquharson [a,*], Michael J. Heap [a], Nick R. Varley [b], Patrick Baud [a], Thierry Reuschlé [a]

[a] Laboratoire de Déformation des Roches, Équipe de Géophysique Expérimentale, Institut de Physique de Globe de Strasbourg (UMR 7516 CNRS, Université de Strasbourg/EOST), 5 rue René Descartes, 67084 Strasbourg cedex, France
[b] Facultad de Ciencias, University of Colima, Colima 28045, Mexico

ARTICLE INFO

Article history:
Received 22 January 2015
Accepted 30 March 2015
Available online 7 April 2015

Keywords:
Andesite
Permeability
Porosity
Field study
Volcán de Colima
Physical properties

ABSTRACT

Permeability of the edifice is one of the key parameters governing eruptive style, magnitude, and frequency of active stratovolcanoes. This study presents a suite of density and permeability field measurements from 572 samples of edifice-forming andesite from Volcán de Colima, Mexico. The breadth of the density distribution of the rocks collected (corresponding to porosity values from 2.5 to 73%), and the increasing bimodality towards the vent, are indicative of the explosive–effusive behaviour that characterises active composite volcanoes. Measured field permeabilities are in the range of 10^{-16} to 10^{-11} m^2, encompassing values significantly greater than those generally assumed for fluid transport in magma, and thus emphasising the importance of host-rock permeability in facilitating outgassing of volatiles and, in turn, governing eruption dynamics. For any given porosity we observe up to four orders of magnitude in permeability. This range of scatter was found to be unaffected for the most part by meso-scale textural differences, oxidation, or alteration. A complementary laboratory and microstructural study reveals that the andesites collected are microstructurally diverse and complex. For example, anomalously high surface areas are measured in samples with significant inter-microlite microporosity. However, these micropores do not serve to significantly increase porosity or pore connectivity, resulting in underestimation of fluid pathway tortuosities using the Kozeny–Carman relation. Indeed, calculated tortuosity values highlight that the Kozeny–Carman relation poorly predicts connectivity and does not therefore capture the microstructural complexity of the studied volcanic rocks. A changepoint porosity value, where the permeability–porosity power-law exponent changes, is identified at around 14% porosity using a Bayesian Information Criterion analysis. Here we assume a change in the dominant microstructural element controlling fluid flow, i.e. from crack- to pore-dominated flowpath geometries. Microstructural analysis indicates that fluid flow in the low porosity andesites (<14%) of this study is governed by tortuous microcracks, while the more porous samples (>14%) display relatively large, interconnected pores. While the supposition that the power-law exponent changes at a distinct changepoint is a simplification, we find that it well describes permeability data from Volcán de Colima (from this study and those of previous authors). The exceptional heterogeneity of edifice-forming rocks is thought to have significant implications for lateral outgassing, eruption dynamics, as well as influencing regional edifice strength and stability.

1. Introduction

1.1. Permeability of a volcanic edifice

Permeability, quantifying the capacity of a material to transmit fluids, is fundamental in controlling a variety of processes in geological systems, and can vary over twelve orders of magnitude in natural rocks (Guéguen and Palciauskas, 1994). In volcanic settings, permeability is a key parameter controlling eruptive style and magnitude by influencing the capacity for a volcano to outgas (Jaupart, 1998; Edmonds et al., 2003; Costa, 2006; Taisne and Jaupart, 2008; Castro et al., 2014). As magma ascends, volatile species exsolve (degas) from the melt phase due to oversaturation; the relative ease by which these volatiles can then outgas depends on the permeability of the rocks forming the edifice (e.g., Jaupart, 1998), and the connectivity and mobility of bubbles in conduit magma (i.e. outgassing through a permeable network in the magma, e.g., Plail et al. (2014); Shields et al. (2014)). Efficiently degassed and outgassed magma tends to erupt effusively (e.g. Lev et al., 2012), constituting a hazard only in the immediate vicinity of a volcano. On the other hand, inefficient outgassing can result in volatile

* Corresponding author.
E-mail address: farquharson@unistra.fr (J. Farquharson).

http://dx.doi.org/10.1016/j.jvolgeores.2015.03.016
0377-0273/

oversaturation and pressure build-up within the volcano, ultimately fostering catastrophic explosive eruptions, flank collapse, and pyroclastic density currents (e.g. Wallace and Anderson, 2000). In these latter cases, impacts may be widespread, long-lived, and lethal.

Stratovolcanoes comprise an edifice constructed by indiscriminate emplacement of explosive and effusive products, surrounding a central magma conduit or cluster of dykes (e.g., Biggs et al., 2010; Gudmundsson, 2012). Continual accumulation of these products results in a structure with spatially variable physical properties, with pervasive differences in porosity and permeability down to the intra-clast scale. Thus transport networks for magmatic volatiles are dependant not only on large-scale fault systems (which may not necessarily provide a direct pathway for volcanic gas species: see Varley and Taran (2003)), but also on the fluid transport properties of the constituent edifice-forming rocks.

Models of volcanic processes must be built on a foundation of observed or experimentally derived parameters; however, as we often wish to understand fluid flow in regions of the edifice that are difficult or indeed impossible to access, permeability cannot necessarily be determined in situ. It is thus of importance to relate transport properties of porous volcanic rocks to the governing physical properties, such as porosity. Though it is evident that the capacity for fluid transport through a porous rock is somewhat dependent on its connected pore space (porosity φ), it is nontrivial to define a precise relationship due to the microstructural complexity of the medium involved (e.g. Zhu and Wong, 1996; Bernabé et al., 2003). Generally, permeability k is estimated as some function of connected porosity, such that $k = f(\varphi)$, where f may include further parameters such as tortuosity (τ) or pore aperture radius. This relation then forms the basis of permeability modelling reliant on empirical or semi-empirical Kozeny–Carman equations (geometrical models), or network modelling (statistical models) (see Guéguen and Palciauskas (1994) for a review).

It is recognised that no all-encompassing theory exists to describe this relationship in all media, due primarily to the fact that some pore geometries may be more effective than others at transporting fluid (e.g. Bernabé et al., 2003). Nevertheless, models such as the Kozeny–Carman (see Kozeny (1927); Carman (1937)), or percolation theory (Sahimi, 1994) have been employed and modified in order to describe the behaviour of volcanic rocks (e.g. Klug and Cashman, 1996; Klug et al., 2002; Mueller et al., 2005; Costa, 2006). In turn, estimates of permeability can be included in numerical simulations of various volcanic processes, with the ultimate aim of predicting the behaviour of a given volcanic system (e.g. Lacey et al., 1981; Day, 1996; Clarke et al., 2002a, b; Reid, 2004; Collinson and Neuberg, 2012; Lavallée et al., 2013).

Previous experimental studies concerning the permeability and porosity of volcanic rocks (e.g. Eichelberger et al., 1986; Klug and Cashman, 1996; Tait et al., 1998; Saar and Manga, 1999; Blower, 2001; Klug et al., 2002; Melnik and Sparks, 2002; Sruoga et al., 2004; Mueller et al., 2005; Wright et al., 2006; Bernard et al., 2007; De Maisonneuve et al., 2009; Yokoyama and Takeuchi, 2009; Heap et al., 2014a,b; Gaunt et al., 2014; Okumura and Sasaki, 2014) have highlighted a vast range of measured values. Porosity of the various volcanic materials—as determined in these laboratory-based studies—has been shown to range between 3 and 90%, while permeabilities in the range of 10^{-17}–10^{-8} m^2 have been measured. The spatiotemporal variation of the physical properties of volcanic rocks necessitates the sampling of a statistically robust dataset (Kueppers et al., 2005; Bernard et al., 2015). In light of these factors, the research herein comprises a systematic field campaign assessing the permeability of edifice-forming rocks representative of a typical andesitic volcano. Combined with field-based density measurements and a complementary laboratory-based study, we further explore the microstructural processes governing permeability in volcanic rocks. While we focus herein on cooled, variably fractured rock, the incidence of fracturing in magma—for example due to strain localisation close to the conduit margins (e.g. Lavallée et al., 2013; Gaunt et al., 2014)—means that the following discussions and conclusions may also be extended to outgassing processes at the periphery of the conduit, as well as in the edifice.

1.2. Case study: Volcán de Colima

Volcán de Colima is situated at 19°30′45.82″N, 103°37′2.07″W on the Colima–Jalisco border at the south-western margin of the Trans-Mexican Volcanic Belt (Fig. 1). Along with the extinct Nevado edifice, the volcano comprises the Colima Volcanic Complex, marking the conjunction of the Colima rift zone and the Tamazula fault (Rodríguez-Elizarrarás, 1995; Norini et al., 2010). Overlying a Cretaceous basement consisting of deformed volcanic and sedimentary rocks (Rodríguez-Elizarrarás, 1995), Volcán de Colima forms a typical stratocone, with eruptive products varying little in bulk composition: crystal-rich andesites with SiO_2 contents typically between ~58 and 61 wt.% (Luhr, 2002; Mora et al., 2002; Valdez-Moreno et al., 2006; Reubi and Blundy, 2008; Savov et al., 2008). Historic volcanism has been characterised by periods of effusive activity (dome formation and lava flows, determined by magma ascent rates, topography, etc.), punctuated by frequent Vulcanian explosions and commonly culminating in voluminous Plinian eruptions (e.g. Luhr, 2002; Varley et al., 2010; James and Varley, 2012; Lavallée et al., 2012). The most recent period of sustained activity began in January 2013, consisting of dome extrusion, pyroclastic density current generation, and intermittent Vulcanian activity. As of April 2015, frequent explosive events were still ongoing.

Volcán de Colima exhibits many characteristics common to convergent margin volcanoes, such as Santa Maria (Guatemala), Ruapehu (New Zealand), Lascar (Chile), Mount Merapi (Indonesia), Citlaltépetl (Mexico), or Egmont Volcano (New Zealand): the steep conical edifice structure overlying a sedimentary basement (e.g. Carrasco-Núñez, 2000; Smyth et al., 2005; Gaylord and Neall, 2012) fosters frequent collapse events (e.g. Rose et al., 1977; Gardeweg et al., 1998; Gamble et al., 1999; Camus et al., 2000; Carrasco-Núñez, 2000), with cyclic eruptive behaviour interspersed with periods of dome effusion (e.g. Rose et al., 1977; Houghton et al., 1987; Gardeweg et al., 1998; Gamble et al., 1999; Camus et al., 2000; Carrasco-Núñez, 2000; Gaylord and Neall, 2012). Combined with its consistently intermediate composition, we maintain that Volcán de Colima can be viewed as generally representative of andesitic stratovolcanoes worldwide.

2. Methods

2.1. Field methods

We collected 572 hand samples from sites around the volcano, shown in Fig. 1, comprising over half a metric ton of andesitic edifice rock. The sites are debris-flow tracks, locally termed *barrancas*: La Lumbre, Montegrande, and El Zarco; as well as a site at El Playón, the area between the summit cone and the ancient caldera wall (Fig. 1). These sites were chosen due to their accessibility and because they all contain abundant loose surface material of a size suitable for our methods (i.e. approximately fist-sized clasts). The collected samples comprise a range of variably remobilised and reworked explosive and effusive products, representative of the edifice-forming materials. A portable air permeameter (Vindum Engineering TinyPerm II) was used to measure the permeability of each hand sample. By evacuating air from a rock, the TinyPerm II unit calculates a value based on the monitored response function of the transient vacuum at the nozzle-rock interface, which corresponds to the sample permeability. The relation between the given TinyPerm value and Darcian permeability is discussed in Appendix A.

The ability to make autonomous and rapid measurements is extremely useful when working in the field; as such these permeameters have seen increasing use in volcanology and related geoscience disciplines (e.g. Possemiers et al., 2012; Invernizzi et al., 2014; Vignaroli

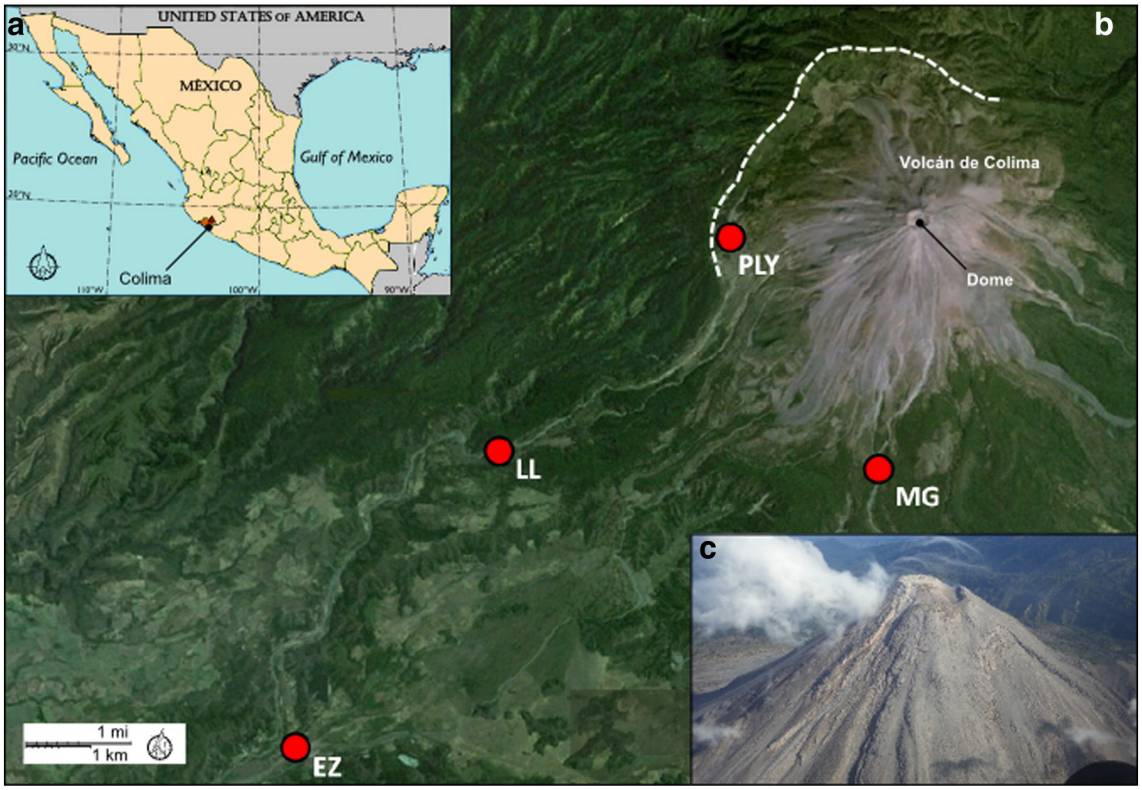

Fig. 1. Volcán de Colima. Inset (a) gives location of Volcán de Colima, (b) shows sample collection sites El Playón (PLY), Montegrande (MG), La Lumbre (LL), and El Zarco (EZ). Active dome and the ancient caldera amphitheatre (dashed line) are also shown. Map is a composite of Google Earth™ imagery (19°30′45.82″N, 103°37′2.07″W). Inset (c) is an aerial photograph of the active summit area, taken on 3rd June, 2014.

et al., 2014). For this reason, Appendix A also includes systematic assessment (comprising 400 measurements) of the capabilities, accuracy, and repeatability of a TinyPerm unit.

Permeability anisotropy in volcanic rocks has been discussed by several authors (e.g. Clavaud et al., 2008; Wright et al., 2009; Gaunt et al., 2014), resulting as a function of anisotropic bubble growth and crack propagation during ascent, eruption, and emplacement of volcanic materials. In laboratory measurements, the pathway for fluid flow can be approximated as we peripherally confine a cylindrical sample and control the rate of flow or the up- and downstream pressures. The field process, on the other hand, involves the evacuation of irregularly shaped, unconfined samples, meaning that measurement is nominally isotropic, even if the actual permeability of the sample is not. As the edifice is constructed of rocks chaotically oriented with respect to any existing anisotropy, we measured field permeability on an average of three faces for each sample (where this was possible: given the heterogeneous shape and size of the hand samples, this procedure was not always feasible). This further ensured a robust methodological procedure.

Bulk rock density was also determined for each sample using an Archimedean weighting method similar to that employed by Kueppers et al. (2005). Our method differs in that it accounts for imbibition in the post-processing stage, rather than during the measurement itself: specifically, Kueppers et al. (2005) vacuum-sealed samples in plastic bags to avoid the imbibition of water. The setup consisted of a balance mounted on a tripod, with a water-filled bag suspended underneath (Fig. 2). A windbreak was used in the field in order to minimise the effects of wind on the balance. The balance, with a precision of 0.1 g and a load limit of 5000 g, was used to measure the weight of the rock in air (point 1 in Fig. 2), and the apparent immersed weight taken in a sample basket (point 2). Assuming the fluid (water) density to be 1000 kg m^{-3} (1 g cm^{-3}), then bulk rock density ρ can be determined from the Archimedes principle, such that:

$$\rho = \frac{W}{W - W_I} \quad (1)$$

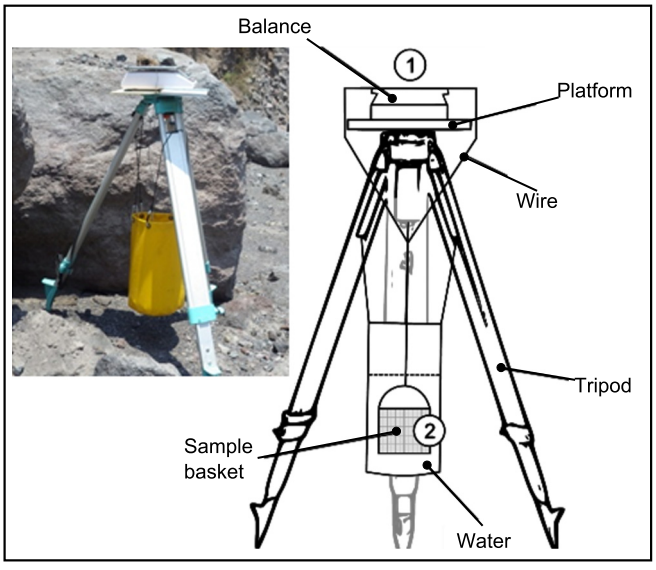

Fig. 2. Schematic of the field setup for measuring sample density (inset shows a photograph), based on the method employed by Kueppers et al. (2005). Weight measurements are performed at points 1 and 2 (see text for discussion). Bag provided by Landjoff Ltd.

where W is weight in air, W_I is the apparent immersed weight, and the denominator is hence equal to the weight of displaced fluid. Measurements of density were subsequently transformed into porosity data; full details are presented in Appendix B. A limit to this method arises in the measurement of some highly pumiceous samples: highly porous pyroclasts with a specific gravity <1 could not be immersed in water due to their buoyancy. While samples could be weighed down with an object of known mass, this method was not employed in this study, mainly due to the fact that so few ($n = 7$) of these highly pumiceous samples were observed in our study areas.

In addition to quantitative measurements, each hand sample was also categorised in terms of visible alteration or structure, or differences in colour; examples of each of these categories are given in Fig. 3. In order to be of practical use in the field, classifications are based on differences readily discernible in hand samples, as such none of the following descriptors are used with a compositional or genetic connotation. "Pumiceous" samples are defined by their high vesicularity, low density, and pale grey colour (Fig. 3c). Samples containing an abundance of large pores and being dark grey to black in colour are referred to as "scoracious", although these textures can extend to lower porosities as well, and occasionally exhibit additional comagmatic features (Fig. 3d). Volcanic material that cannot be texturally described as pumiceous or scoracious is simply referred to hereafter as "lava" (Fig. 3b). "Lava" is generally grey aphanitic to porphorytic juvenile andesite; however rocks in these three categories could also display a variable degree of alteration, including oxidation (examples of which are given in Fig. 3e–h).

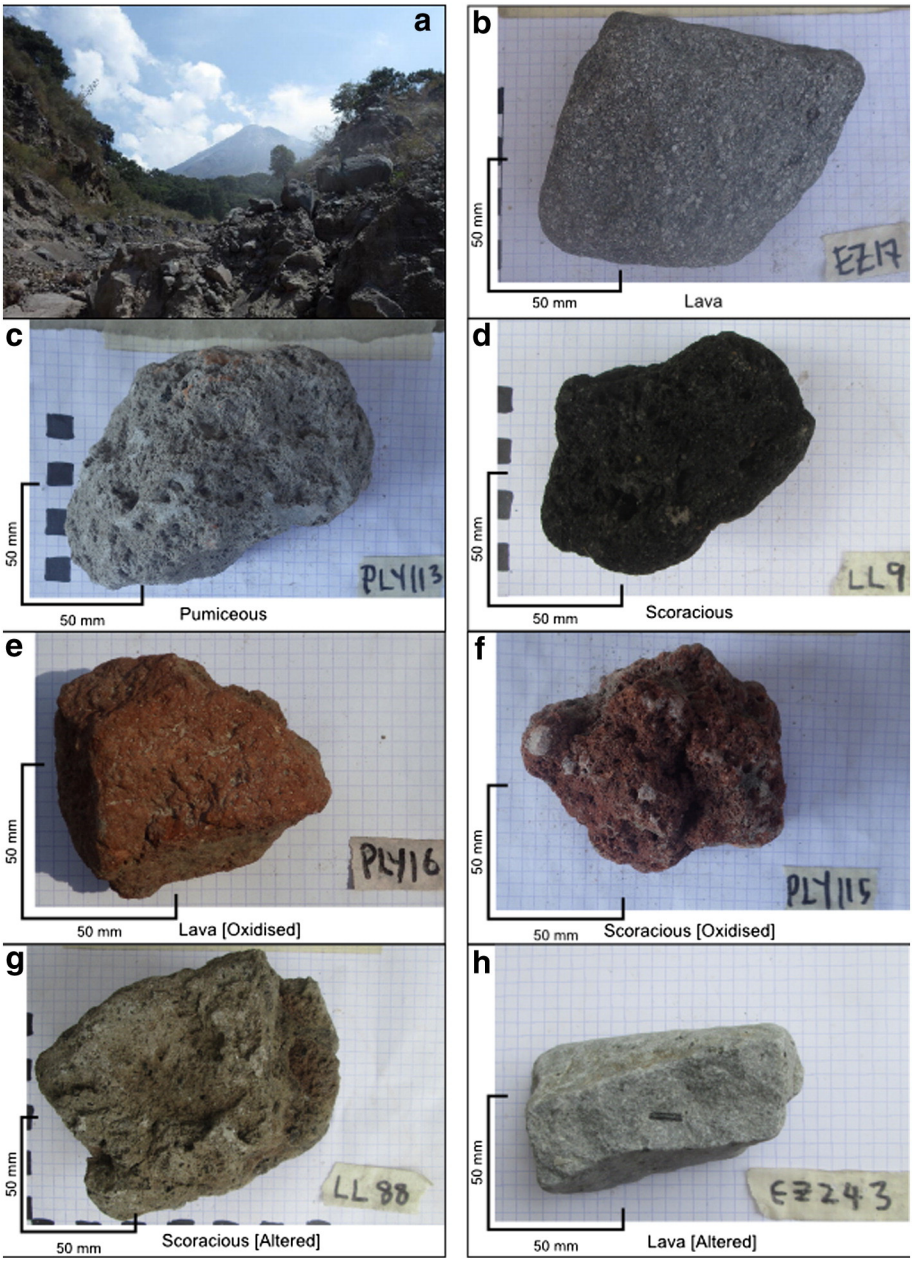

Fig. 3. Rock classification scheme. (a) Barranca Montegrande, a representative debris-flow-track from which samples were collected. Summit of Volcán de Colima can be seen in the background. (b) Pristine porphyritic lava. (c) Pumiceous pyroclast. (d) Scoracious sample, characterised by large, variably elongated pores (vesicles), and typically dark in colour, (e) and (f) show oxidised samples, as evidenced by their brick red colour. Texturally (f) is described as scoracious, respectively. (g) and (h) both show examples of altered clasts: in (g) significant post-emplacement weathering can be observed; in (h) evidence of hydrothermal vapour-phase alteration can be seen. (For interpretation of the references to colour in this figure legend, the reader is referred to the web version of this article.)

Alteration is also manifest in general weathering of the rocks (e.g., due to rainfall, fluvial reworking, and other transport processes), as well as mineral phase replacement resulting from hydrothermal processes (John et al., 2008; Lavallée et al., 2012). The strong correlation between connected porosity and density determined in the following section attests to there being very little variation in bulk composition across the range of samples (see Appendix B).

2.2. Laboratory methods

To complement the field study, a selection of samples was collected to be analysed in the Experimental Geophysics laboratory at Université de Strasbourg. Not only does this afford a more robust exploration of their physical properties and the opportunity to image their microstructure, but also allows us to access permeability data in a range below that measurable by the TinyPerm unit. Based solely on their density, eleven rocks were sub-sampled from the entire dataset to represent the range of porosities observed in the field. Variations in texture or permeability were not considered at this point (the selection process was thus a stratified-random sampling method). Seventeen cylindrical cores, 20 mm in diameter, were obtained from the sub-sample set and precision ground to a nominal length of 40 mm. Connected water porosity was measured for each core using the triple-weight water saturation method (Guéguen and Palciauskas, 1994), and connected gas porosity and skeletal density were measured using helium pycnometry (AccuPyc II 1340). Total porosity (φ_T) was determined as $1 - (\rho_B/\rho_S)$, i.e. the ratio of bulk and skeletal densities for each sample, allowing unconnected porosity (φ_U) to be calculated as $\varphi_T - \varphi$. The double-weight field method was also tested in the laboratory by performing an equivalent set of measurements (i.e. dry mass and apparent immersed dry weight), shown in Appendix B (Fig. B1). Gas permeability of each oven-dry (vacuum dried at 40 °C) core was measured using a benchtop steady-state permeameter. All measurements were performed under 1 MPa confining pressure in order to preclude fluid (nitrogen) flow around the sides of the sample. Samples were left for at least one hour prior to measurement to ensure microstructural equilibration. Volumetric flow rate measurements were taken (using a gas flow meter) under several pressure gradients to determine the permeability using Darcy's law, and to assess the need for the Klinkenberg or Forchheimer correction, which were applied where appropriate. It should be noted that cores were obtained in only one direction from each of the 11 hand samples; consequently, the subsequent analyses and discussion do not account for potential anisotropy in these rocks. Hydraulic radii of samples were determined with Brunauer, Emmett, and Teller krypton adsorption (BET), in order to use the modified Kozeny–Carman relation (after Heap et al. (2014a)) to assess microstructural controls on the permeability of these rocks. The revised Kozeny–Carman equation can be shown as (Yokoyama and Takeuchi, 2009; Heap et al., 2014a):

$$k_{KC} = \frac{\varphi^3}{b\tau^2 \rho_B{}^2 S_{BET}{}^2} \quad (2)$$

where ρ_B is bulk density, S_{BET} is the specific surface area, and b is a geometric constant. Assuming that porosity is either crack-controlled ($b = 12$), or a pore-controlled ($b = 8$) (Bernabé et al., 2010) we can thus solve for tortuosity τ.

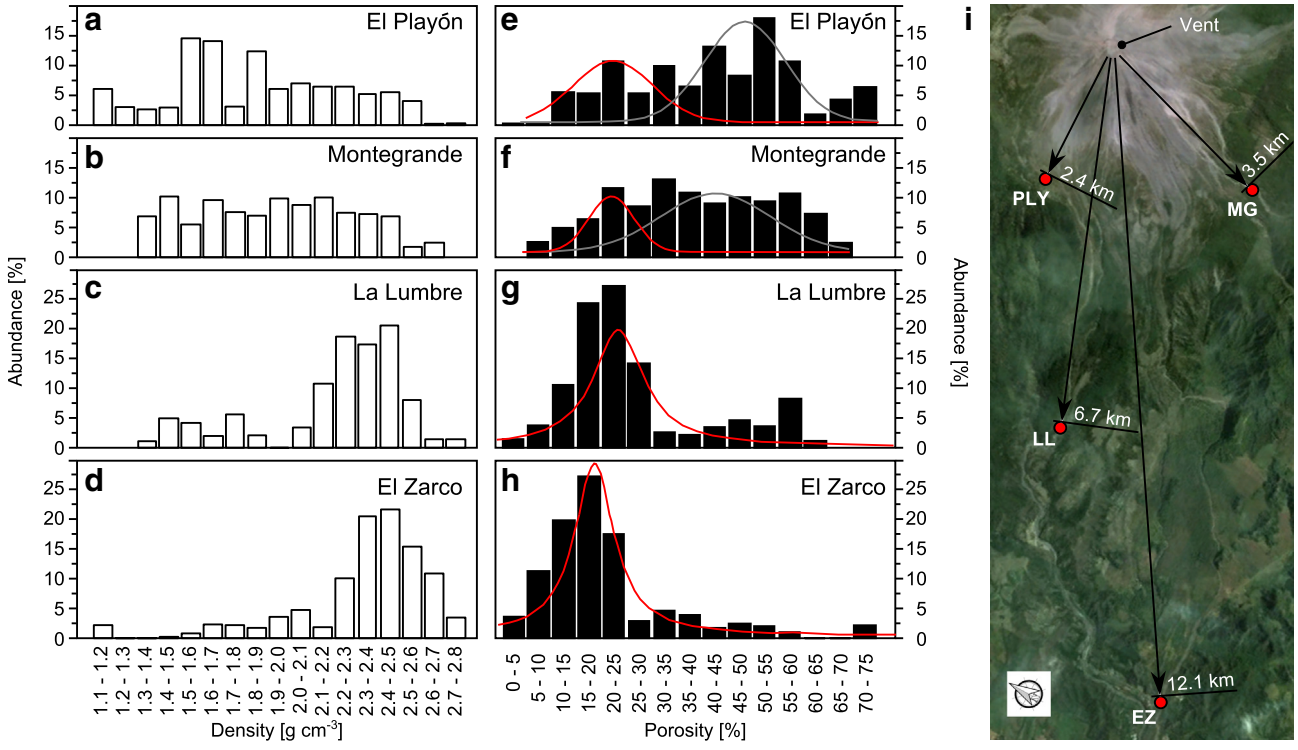

Fig. 4. (a)–(d) show the density distribution of collected samples for each of the collection sites. (e)–(h) shows the porosity distribution across the sample sites. Data are shown in terms of their weighted abundance, after Bernard et al. (2015). The map (i) indicates the distance of each site from the active vent. Note that distance indicated is the minimum transport distance (i.e. straight-line distance). PLY = El Playón; MG = Montegrande; LL = La Lumbre; EZ = El Zarco. Peaks in the low-end of the porosity distributions are described by the red curves. High-porosity peaks are shown by grey curves. For El Playón and Montegrande, the distribution is bimodal; La Lumbre and El Zarco show increasingly skewed distributions. Curves fitted using Origin® data analysis software. Data comprises 118, 94, 97, and 232 samples at each study site, respectively. (For interpretation of the references to colour in this figure legend, the reader is referred to the web version of this article.)

3. Results and discussion

3.1. Density distribution from the vent

Of the 572 collected samples, density could not be determined for samples too buoyant for our field density method. Fig. 4 shows the density (a–d) and porosity (e–h) of the remaining samples collected at each of the sampling sites shown in (i) (also Fig. 1). Relatively uniform or bimodal distributions in density and porosity are seen at the site closest to the active summit region (i.e. El Playón), while the distribution becomes unimodal and notably skewed towards high densities (low porosities) as one moves to sites increasingly more distal: Montegrande, La Lumbre, and El Zarco, respectively. This phenomenon has been noted in previous field studies (e.g. Kueppers et al., 2005), and can be attributed to the increased transport distance and associated degradation of more friable, porous materials. As volcanic deposits are remobilised away from the vent, higher-porosity rocks will be preferentially comminuted into smaller size classes by processes such as abrasion, collision, and fluvial reworking (as shown experimentally by Manga et al. (2011); Kueppers et al. (2012)). As such, the proportion of relatively dense rocks should increase with distance from the vent, as we observe in our data.

The array of porous media collected and measured in the course of this study indicates that edifice material (and hence, the edifice of Volcán de Colima) exhibits extraordinary heterogeneity in terms of its physical properties. A wide range of densities can be observed in the dataset ($n = 542$), from 1142.40 to 2813.79 kg m^{-3}, indicating a correspondingly broad variance in porosities (2.5–72.7%). The porosity within volcanic materials can either be in the form of cracks (due to thermal, mechanical, or chemical stresses) or pores, the frozen-in relicts of bubble formation, growth, and coalescence. As the volatile content in magma comprises one of the fundamental driving forces of explosive activity, the post-eruptive porosity allows us to glean insight into the eruption dynamics and pre- and syn-eruptive conditions within the conduit (e.g. Cashman et al., 1994; Kueppers et al., 2005; Gonnermann and Manga, 2007; Mueller et al., 2011). A tendency towards relatively high porosity values (e.g. as observed at El Playón: Fig. 4e) is indicative of deposits of predominantly explosive origin, while low-porosity rocks are associated with predominantly extrusive material (Cashman et al., 1994; Mueller et al., 2011); the range of measured porosities thus attests to the array of observed eruption styles at Volcán de Colima (e.g. Bretón-González et al., 2002; Mueller et al., 2011). Variability of host-rock porosity also exerts a significant influence over strength and deformation modes within the edifice, in turn affecting outgassing through the edifice and flank stability (Heap et al., submitted for publication). As such, it is imperative that future models of volcanic processes—such as conduit outgassing or mechanical stressing of the edifice—account for the potential diversity of the physical rock properties which underpin these processes.

The density distribution of the erupted material at Volcán de Colima over time is best approximated by that of samples measured at El Playón, closest to the active summit crater: Fig. 4 shows that this distribution is bimodal. If we assume that the initial volatile content of magma is roughly equivalent through time, we can surmise that—in general—dense rocks result from efficiently outgassed magma, likely to have erupted effusively. On the other hand, the lower density peak represents inefficient outgassing of magma and the retention of explosive potential energy. The low porosity and permeability of dense

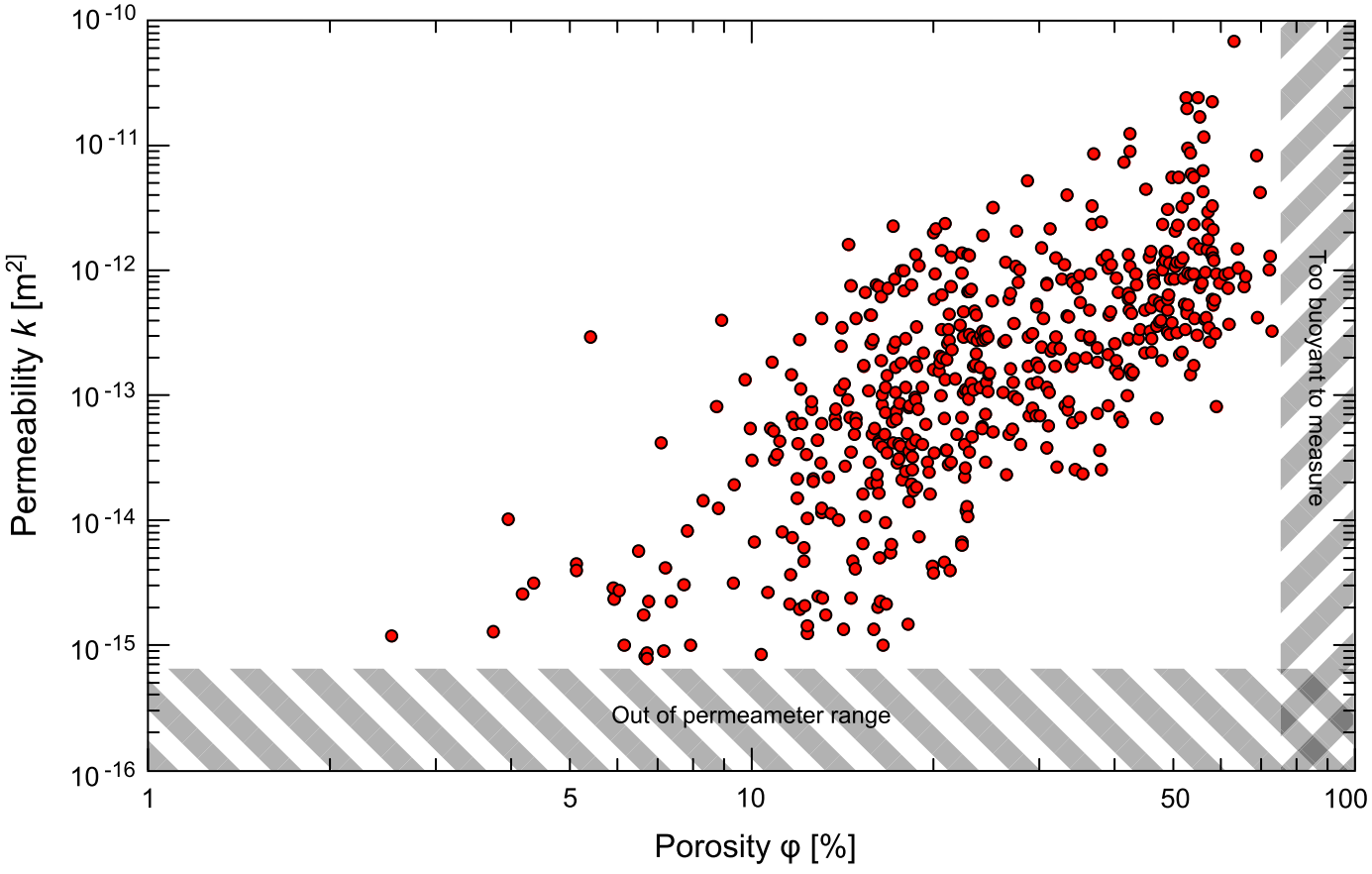

Fig. 5. Permeability–porosity data for 542 samples (i.e. excluding the 30 samples which were either too buoyant to obtain a density measurement, or have a permeability below the limit of field permeameter) across all sample sites and all classifications, as measured in the field. Hatched areas indicate regions where the field methods were ineffective, either because sample permeability was below the limit of the permeameter, or because samples were too buoyant to measure using the double-weight method outlined in the text. Each point is a mean value from multiple measurements, as discussed in the text.

lavas will consequently limit outgassing, resulting in the eruption of less dense material. In turn, this material will increase the permeability of the edifice, fostering extrusion of dense products, and so the cycle continues. Thus, explosive decompression and fragmentation serve to facilitate outgassing in future eruptive cycles (e.g. Gonnermann and Manga, 2003). It is probable that the range of porosities is therefore linked to the frequency and cyclicity of highly explosive eruptions at Volcán de Colima (e.g. Robin et al., 1991; Luhr, 2002), and at least partially dictates the observed transition between explosive and effusive behaviours.

Further, previous works have shown that porosity has a significant influence on the strength and failure mode of volcanic rocks (e.g. Zhu et al., 2011; Heap et al., 2014a). The increased proportion of high-porosity material near the vent and proximal flanks of the volcano will consequently decrease stability in this region, leading to more frequent, local slope failure than observed distal to the vent.

3.2. The relationship between porosity and permeability

The initial dataset of 572 hand samples contained 30 samples which were either too buoyant to measure porosity or of a permeability too low to measure permeability in the field: the lower limit of the field permeameter (6.92×10^{-16} m^2) did not permit measurements of permeability for some of the very low porosity samples. Samples for which a value for either porosity or permeability could not be obtained are not included in any further analysis. Transformed field data are displayed in Fig. 5: our data show that there is a general trend of increasing permeability with increasing porosity. Porosity values range from 2.5 to 72.7%, while permeabilities lie between 7.6×10^{-16} and 6.5×10^{-11} m^2.

For rocks of comparable porosity, a difference in permeability of up to four orders of magnitude can be observed, as has been noted in previous studies of volcanic materials (e.g. Saar and Manga, 1999; Klug et al., 2002; Mueller et al., 2005; De Maisonneuve et al., 2009; Wright et al., 2009; Yokoyama and Takeuchi, 2009). Notably, comparable values of permeability can also be associated with rocks with very different porosities. While part of this distribution may be explained by permeability anisotropy (as discussed previously; see e.g. Clavaud et al. (2008); Wright et al. (2009); Gaunt et al. (2014)), microstructural attributes such pore geometry will contribute significantly to permeability. For instance, a rock with a single through-running crack could have a very low porosity, while providing an effective fluid conduit. On the other hand, a rock structure consisting of many large pores connected by tortuous microcracks could be poor at transmitting fluids, despite having a relatively high porosity. It is important to note that the edifice is haphazardly constructed of variably porous material with differing eruptive and emplacement histories: in reality, a representative suite of edifice-forming rocks is bound to contain both these end-members and a range of more or less effective pore geometries in between (discussed in detail below). Due to this inherent natural variability, it is therefore unsurprising that a large degree of scatter is evident in our field data.

Fig. 6 displays the field permeability data grouped by our rock classification scheme (i.e. lava, scoracious, pumiceous, altered and oxidised). Notably, the degree of scatter observed in Fig. 5 appears to be largely unaffected by meso-scale textural differences, or by syn- or post-eruption alteration. Lava (Figs. 3b, 6a) comprises the

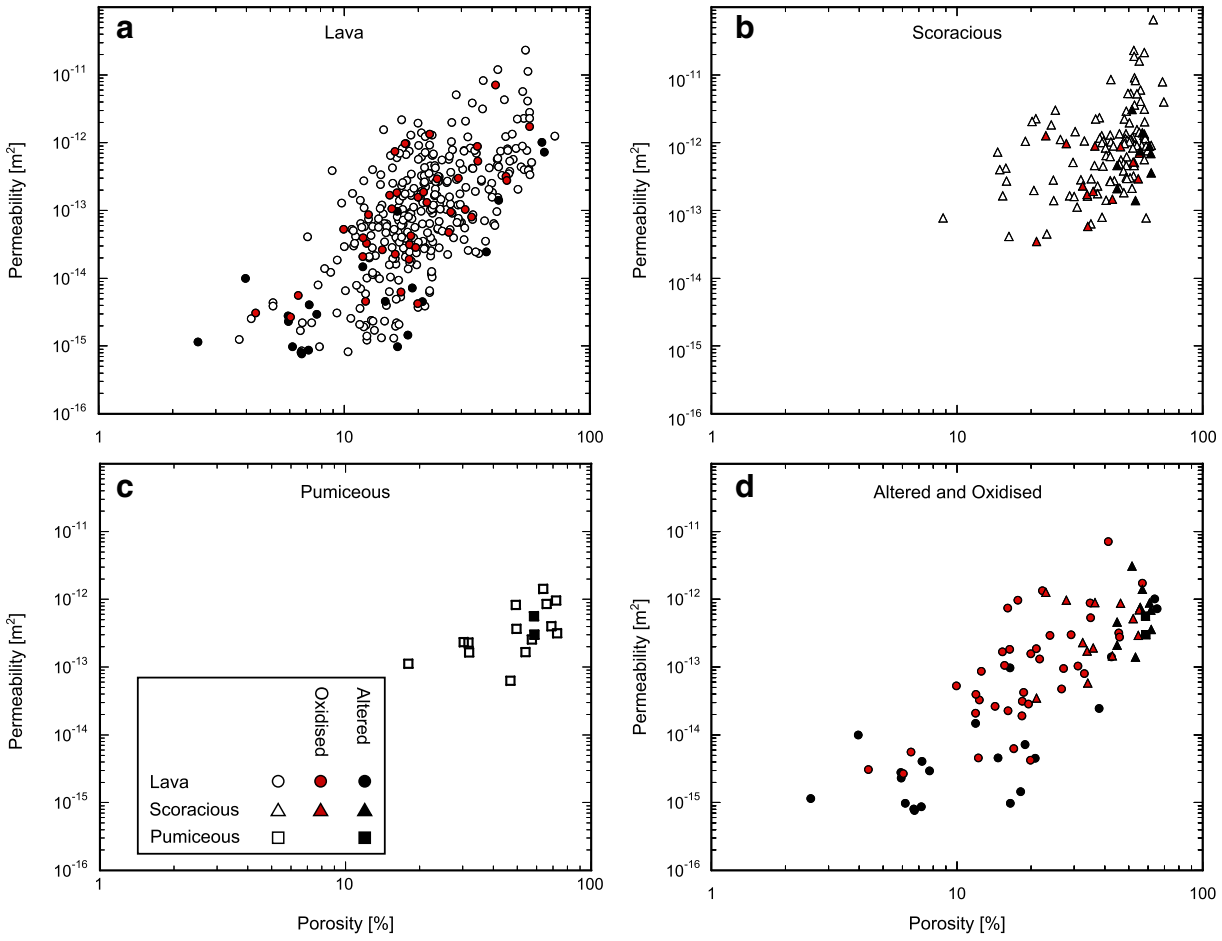

Fig. 6. Field permeability–porosity data sorted by sample classification; a: lava ($n = 390$); b: scoracious material ($n = 136$); c: pumiceous material ($n = 16$); and d: altered (including oxidised) samples ($n = 95$). By definition, scoracious and pumiceous rocks (b, c) occupy only the higher-porosity domain. Lava, altered, and oxidised samples (a, d), on the other hand encompass the whole range of porosities and permeabilities.

majority of field samples ($n = 378$), and encompasses the range of measured permeabilities and porosities. For any given porosity, permeability may differ by up to four orders of magnitude, a phenomenon which is consistent for the oxidised and altered rocks (denoted by the red and black filled symbols, respectively). Scoracious samples (Figs. 3d, 6b) display a similar range of permeability for a given porosity, with porosities of around 60% yielding permeability values from 7.8×10^{-14} to 6.5×10^{-11} m^2. It is possible that the elongation of vesicles associated with scoracious deposits fosters a significant degree of permeability anisotropy, as discussed by Wright et al. (2009). Pumiceous samples (Fig. 3c) show a narrower extent of permeabilities, from 6.3×10^{-14} to 1.4×10^{-12} m^2 (Fig. 6c), however this may merely be a product of their low sample number ($n = 16$) relative to the other classes. While hydrothermal alteration, weathering, or oxidation will influence the porosity and permeability of an individual sample, we note that, following the subdivision of the data into these categories, the general permeability–porosity trend (as observed in Fig. 5) is unaffected, as shown in the synopsis plot of Fig. 6d.

3.3. Volcán de Colima andesites: microstructural complexity

To provide deeper insight into the observed variability in the field samples, we now provide laboratory measurements of physical rock properties (including permeability), and an assessment of the micro-scale complexities in andesites representative of the observed porosity range of edifice-forming rocks. Measuring permeabilities in the laboratory allows us to include samples that would otherwise fall below the measurable limit imposed by the field method. Given that meso-scale textural differences have been shown to explain little of the variation in the field data (Fig. 6), the sample set comprised lava, scoracious, and pumiceous material in order to maximise the porosity range (from 3.5 to 59.4%, in 17 cylindrical cores; see Table 1).

Fig. 7 displays the laboratory-determined values for permeability and connected gas porosity against other measured or calculated physical properties: specific surface area, tortuosity (Eq. (2)), and overall connectivity. To assess the degree of overall pore connectivity within these andesites, we examine the ratio of connected and unconnected porosity for each of our laboratory samples, deriving a dimensionless parameter Γ as a proxy for pore connectivity, such that $\Gamma = 1 - (\varphi_U/\varphi)$. Physical property data for each sample are given in Table 1.

As observed in our field data (Fig. 5), permeability increases with increasing connected porosity (Fig. 7a). We observe that the increase is nonlinear; rather, the data appears to describe a dogleg or kink (in log–log space). This phenomenon is discussed in detail in the following section. Specific surface areas of these andesites appear to fall into two distinct families (Fig. 7b), with the majority of samples containing a specific surface area of less than 100 m^2 kg^{-1}, and showing an increasing trend with increasing porosity. However, for the two samples containing the lowest porosities, we measure much higher surface areas, in excess of 500 m^2 kg^{-1} (Table 1). For perspective, the surface area within a cylindrical sample (EZ_94: length = 41.11 mm; diameter = 19.91 mm) is greater than the area between the goalposts in a football (soccer) goal. Notably, Scanning Electron Microscope (SEM) analysis has shown that the high surface area data are associated with a pilotaxitic groundmass containing abundant high aspect ratio microlites, attributed to syn- and post-eruptive differentiation. Between these microlites we observe micro-scale pore space (microporosity), which we define as pores less than 30 μm in diameter (see Zhu et al., 2010, and references therein). Microporosity can be observed in the SEM photomicrographs of Fig. 8a–c, and serves to greatly increase the internal surface area while contributing little to overall porosity and fluid transport. Samples with only microporosity (e.g. EZ_69; EZ_94) show very low permeabilities (Fig. 7a; Table 1), thus we can infer that micropores may not contribute significantly to fluid transport in the samples with higher permeabilities (see also Saar and Manga (1999)). The fact that a large proportion of the internal surface does not contribute to fluid flow highlights that the permeability of these samples are poorly approximated by the Kozeny–Carman relation (Eq. (2)). In contrast, the specific surface area within sandstone, a rock with a much simpler microstructure, has been shown to correspond strongly with both porosity and permeability (e.g. Rabbani and Jamshidi, 2014).

Calculated tortuosities of all samples were low ($0 < \tau < 2.2$), with the majority <1 (Fig. 7c; Table 1). In reality a tortuosity less than one is impossible (this representing a perfectly straight flow path); however, values in this range have been predicted previously for volcanic rocks, such as highly-porous andesite (Heap et al., 2014a), and rhyolitic pumice (Degruyter et al., 2010; Wright et al., 2009). In contrast to Heap et al. (2014a) however, we do not observe high tortuosities at values of low connected porosity. It is a peculiarity of our data that the anomalously high surface areas cancel out the effects of low connected porosity when using Eq. (2), yielding low tortuosity values. Even disregarding these two values, we note that internal surface area alone does not appear to exert a dominant control on permeability and is thus a poor predictor of permeability in the volcanic rocks of this study (Fig. 7d).

Overall connectivity Γ lies between zero and one, where zero represents a pore network completely isolated from the outside of the sample, and one corresponds to a sample where all of the porosity is connected. Fig. 7e shows the relation of this parameter to connected porosity (on linear axes), while Fig. 7f illustrates the

Table 1
Physical properties of a suite of Volcán de Colima andesites, including porosity, bulk density, specific surface area, permeability, tortuosity, and connectivity. Tortuosity has been calculated according to Eq. (2), assuming $b = 8$ or 12 (see text for discussion). Letter in brackets refers to sample classification: L = lava; S = scoracious; P = pumiceous.

Sample	Connected porosity φ [%]	Unconnected porosity φ_U [%]	Connectivity Γ	Bulk density ρ_B [kg/m^3]	Specific surface area S [m^2/kg]	Permeability k [m^2]	Tortuosity τ
EZ_120 (L)	18.5	1.7	0.91	2139.32	28	2.72×10^{-13}	0.90
EZ_121 (L)	9.6	0.3	0.97	2454.39	18	6.05×10^{-14}	0.79
EZ_69 (L)	4.6	1.1	0.76	2670.47	522	1.62×10^{-17}	0.50
EZ_94 (L)	3.5	0.6	0.82	2658.23	546	9.47×10^{-17}	0.13
LL_43a (S)	46.8	0.8	0.98	1422.23	96	4.17×10^{-13}	1.29
LL_43b (S)	48.1	0.9	0.98	1386.71	82	4.48×10^{-13}	1.55
LL_74a (L)	10.6	0.7	0.93	2396.42	59	5.29×10^{-14}	0.31
LL_74b (L)	8.5	0.9	0.90	2448.07	47	1.25×10^{-15}	1.76
LL_96 (S)	44.9	1.7	0.96	1450.14	212	4.37×10^{-13}	0.52
MG_02 (L)	23.4	0.8	0.97	2054.79	36	4.37×10^{-13}	0.82
MG_22a (L)	27.4	<0.1	1.00	1943.45	42	4.39×10^{-13}	0.94
MG_22b (L)	24.5	<0.1	1.00	2024.24	36	4.39×10^{-13}	0.89
MG_28 (S)	46.6	1.0	0.98	1436.68	53	4.67×10^{-13}	2.16
PLY_116a (P)	57.5	2.0	0.96	1094.30	56	3.94×10^{-12}	1.27
PLY_116b (P)	57.9	2.1	0.96	1081.20	70	1.75×10^{-12}	1.56
PLY_116c (P)	59.4	2.0	0.97	1042.74	63	1.40×10^{-12}	2.08
PLY_116d (P)	58.6	2.2	0.96	1060.52	61	1.77×10^{-12}	1.84

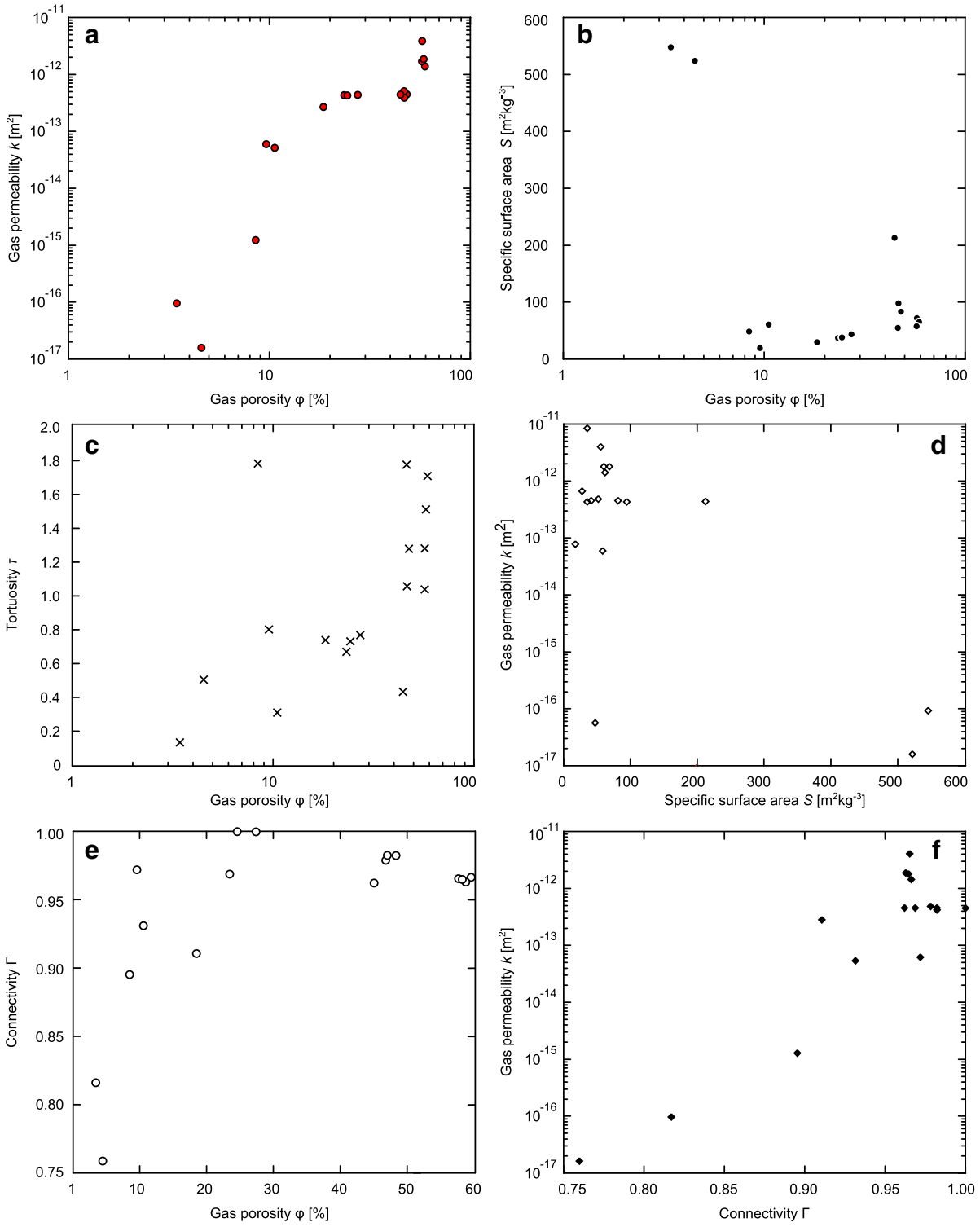

Fig. 7. Physical property data of laboratory samples. (a) shows connected gas porosity against gas permeability on log–log axes. Gas porosity versus specific surface area is given in (b), and tortuosities calculated according to Eq. (2) in panel (c). (d) shows specific surface area against gas permeability. (e) shows pore connectivity, plotted against connected porosity (note that porosity is here shown in a linear axis, in contrast to the logged axes of the other panels. See text for discussion). Finally, (f) displays gas permeability against connectivity in semi-log space.

approximately exponential increase in permeability with pore connectivity. While this parameter affords insight into the degree of connectivity to the outside of the sample, it does not indicate the relative efficiency of each pore interconnection. Ostensibly, measuring properties such as connected porosity or surface area makes use of all available pore space. On the other hand, pathways perpendicular to flow, excessively tortuous, or which involve very narrow pore apertures may be redundant to flow, and thus not included in measurements of permeability.

3.4. A critical porosity: microstructural changepoint

When describing permeability as proportional to integer powers of geometrical parameters (i.e. φ, τ, S), as in Eq. (2), is it generally given

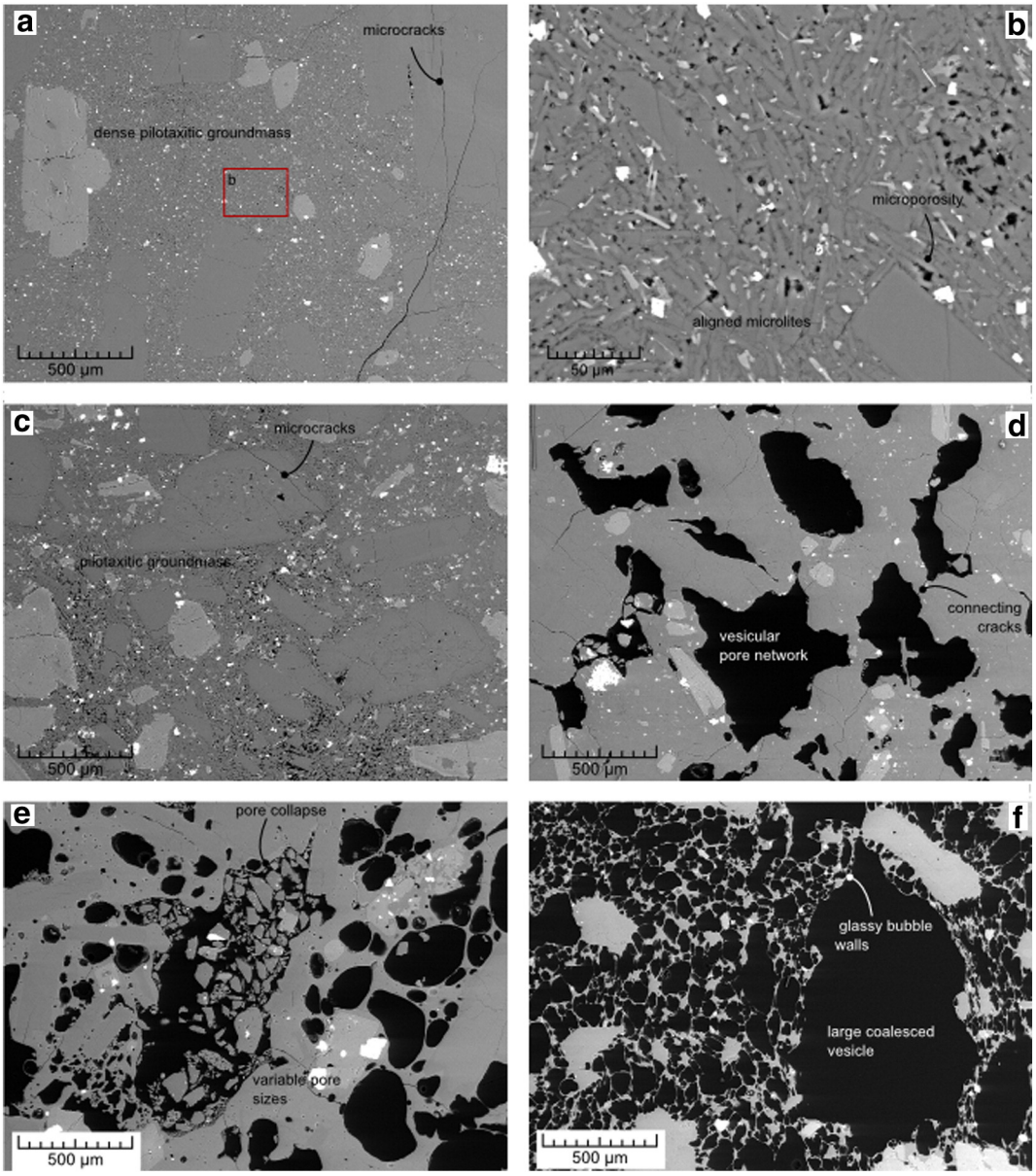

Fig. 8. Microstructures. Scanning electron microscope backscatter photomicrographs of an array of andesites from Volcán de Colima. (a) is from sample EZ94, with a porosity around 3.5%. The sample has a highly dense pilotaxitic groundmass containing thin and tortuous microcracks. Panel (b) shows a close-up view of the abundant microlites in (a), highlighting their flow-alignment and intercrystalline of microporosity. Similar textures can be observed in (c), sample EZ69 (porosity ~5%). The marginally higher porosity may be due to the relatively greater degree of microporosity compared to the samples shown in (a) and (b). The pilotaxitic textures observe in these samples correspond to anomalously high surface area measurements. In (d), a more porous rock (MG22: ~25%) shows large subspherical pores, variably well connected with cracks. Panel (e) shows connected vesicles in a glassy groundmass (sample LL96: ~45%). Finally, (f) shows a pumiceous sample (PLY116: ~58%), with characteristically large pores and thin glassy bubble walls. The sequence of images shows a transition between crack- and pore-dominated geometries (as discussed in Section 3.4).

that these parameters are similarly correlated by power-law relations (Bernabé et al., 2003). We can thus infer that the slope m of a fitted curve is the exponent of the relation $k = f(\varphi^m)$. However, and as seen in Fig. 7a, the assumption that permeability can be simply described by porosity to a single power-law exponent m is false in the case of the andesites of this study. In previous laboratory studies involving physical properties of volcanic rocks (andesites from Volcán de Colima: Heap et al., 2014a; welded block-and-ash flow deposits from Mount Meager, Canada: Heap et al., 2014b), a critical "crossover" porosity, at which the value of m changes significantly, was observed. A crossover porosity has similarly been observed in sandstone (Bourbie and Zinszner, 1985). In each case, the crossover porosity was interpreted as the result of a distinct change in rock microstructure. These studies by Heap et al. (2014a, 2014b) on volcanic materials estimate the threshold value of porosity to exist between 12 and 15%, though this value is assigned on a best-estimate basis. When plotted in log–log space this threshold resembles a piecewise linear model, as has been applied in other geoscientific studies, notably that of Hatton et al. (1994). The piecewise linear model assumes that log transformed data are described by one linear relationship until a defined changepoint (crossover), whereafter data are described by a linear relation with a different slope (correspondingly, the original data may be described by two distinct power-law relations).

The existence of such a changepoint in our field data cannot be definitively argued, the reasons for which are twofold: firstly, data obtained in the field does not extend to lower permeabilities ($<10^{-16}$ m^2). Secondly, any fitted curve is influenced by the porosity distribution of the sample set, which causes the paired permeability–porosity data to cluster between 10 and 25%. However, our laboratory-derived data (and laboratory data of other

authors) are not hindered by either issue, thus we can determine whether a statistically justifiable crossover value exists. As well as data from this study, the following analysis was performed on compiled data from Mueller (2006), Kolzenburg et al. (2012), Kendrick et al. (2013), Richard et al. (2013), and Heap et al. (2014a).

Although increasing the complexity of a model can yield curves that better fit the data (in the sense that the residual sum of squares S_R^2 is minimised), arbitrarily increasing model complexity without accounting for the increased number of model parameters can yield false relationships or models which cannot be generally applied. With this in mind, we adopt the modified Bayesian Information Criterion approach outlined by Main et al. (1999), which enacts a penalty for each additional parameter introduced into the model. We compare the cases of a one- and two-slope model, respectively.

Herein, $y_i = \gamma(x_i) + \varepsilon_i$, for i = 1, …, n, where y_i is the ith iteration of the variable to be predicted (in this case, $\log_{10}k$), $\gamma(x_i)$ is the predicted value of y_i and a function of x_i, the explanatory variable (in this case $\log_{10}\varphi$), and ε_i is an error term. The residual sum of squares is defined as:

$$S_R^2 = \sum_{i=1}^{n}[y_i - \gamma(x_i)]^2 \quad (3)$$

where n is the sample size. The independent x_i, y_i data pairs are resampled using a bootstrapping procedure, and the position of a potential changepoint x^* is determined by piecewise linear regression. The two cases for determining $\gamma(x_i)$ are as follows:

$$\gamma(x_i) = a_0 + b_0(x_i); \mathrm{p} = 3 \quad (4)$$

$$\gamma(x_i) = a_1 + \{b_1 x_i[\forall x_i < x^*]\} + \{x^*(b_1 - b_2) + b_2 x_i[\forall x_i \geq x^*]\}; \mathrm{p} = 5 \quad (5)$$

The simple linear case (Eq. (4)) is described by intercept a_0 and slope b_0, while Eq. (5) comprises an intercept a_1, a slope term b_1 for all values below the changepoint x^*, and a slope b_2, corresponding to the slope for all values equal to or greater than x^*. For each model, p is the number of unknown parameters (including the error term).

As in Main et al. (1999), the information criteria for the linear and changepoint models are given by:

$$BIC_R = L(\mathrm{y}) - \frac{1}{2}p\ln\left(\frac{n}{2\pi}\right) \quad (6)$$

$$BIC(x^*) = L(\mathrm{y}, x^*) - \frac{1}{2}p\ln\left(\frac{n}{2\pi}\right) \quad (7)$$

respectively, where $L(\mathrm{y})$ is the maximised log-likelihood function, given by $-n/2\ln(S_R^2)$. We find, for the data of this study, that $BIC(x^*) > BIC_R$, for values of x^* to be around 1.14, corresponding to a porosity of around 14% and permeability of around 1.8×10^{-13} m^2. For our laboratory data, the difference between Eqs. (6) and (7) is greater than 3; typically this analysis is considered robust if $BIC(x^*) - BIC_R \geq 1$.

Despite the fact that the compiled laboratory data were collected using different permeants, under different pressures, and with different experimental setups and methods, a re-examination of these data using the information criterion analysis described above supports the prediction of a changepoint or crossover. Specifically, $BIC(x^*) > BIC_R$ when x^* is close to 1.18 (around 15% porosity). Fig. 9a and b displays the laboratory data of this study and that of other authors, respectively, indicating the model exponents and changepoint locations. The high-porosity exponent for each dataset is remarkably similar (1.7 and 1.5; Fig. 9). While the lower exponents differ somewhat, this difference is greatly exaggerated by the logged x-axis and the fact that low-porosity data are relatively more scarce in the literature. Importantly, this comparison indicates that a changepoint in the permeability–porosity data is not merely an artefact of our selected laboratory samples. The preceding

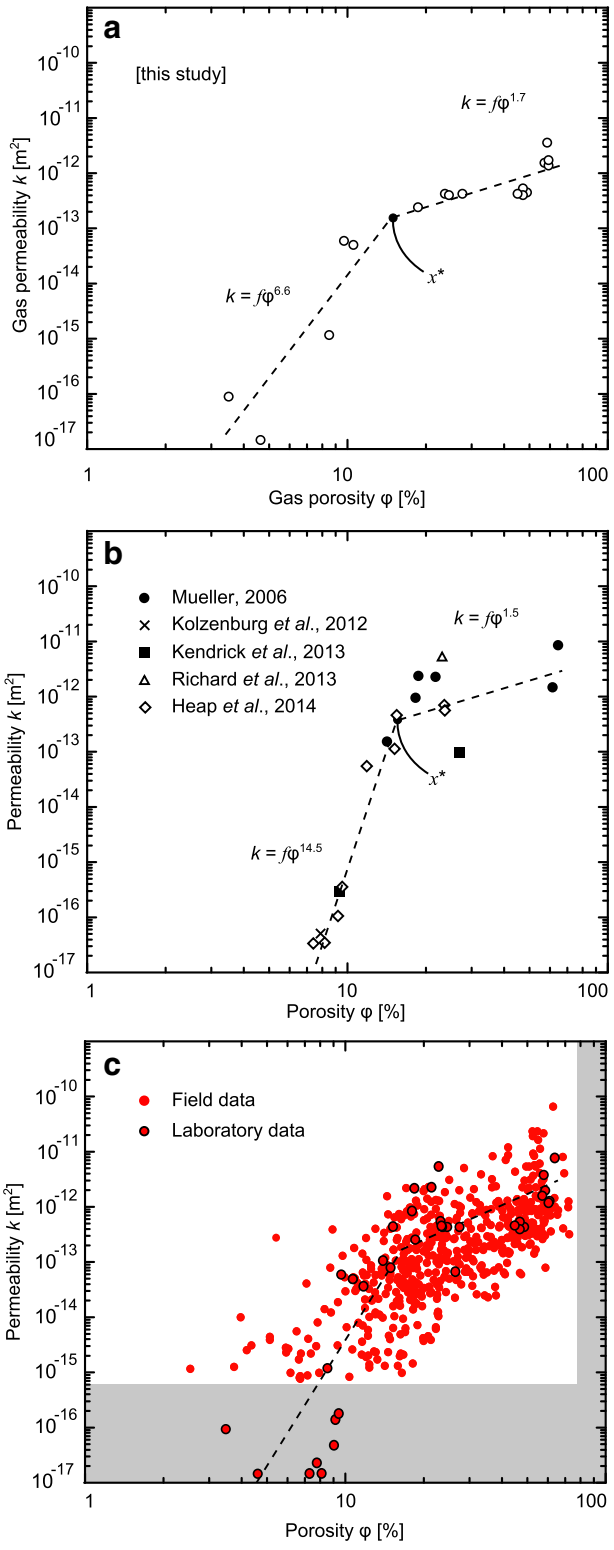

Fig. 9. Microstructural changepoint. Piecewise regression curve fit through the data of this study (a), with the changepoint x^* ~14%. (b) shows compiled Volcán de Colima data from Mueller (2006), Kolzenburg et al. (2012), Kendrick et al. (2013), Richard et al. (2013), and Heap et al. (2014a). Data from Mueller (2006) and Richard et al. (2013) were measured with argon, using the pulse decay method (with an initial pressure differential of 2.5 MPa and 4 MPa, respectively). The Kolzenburg et al. (2012) and Kendrick et al. (2013) data were obtained using water, under a confining pressure of 5 MPa. The data from Heap et al. (2014a) are water permeabilities performed under 2 MPa of confining pressure. The changepoint is maximised at a porosity ~15%. In (c), the field data of this study are overlain with the combined laboratory data of this study and that shown in (b), with a piecewise regression curve derived from the laboratory data ($x^* \approx 16\%$).

analysis is useful as it identifies the porosity (and permeability) where we can expect to observe a significant change in microstructure. The differences discernible between the SEM photomicrographs in Fig. 8a–c (below the changepoint) and Fig. 8d–f (above the changepoint), are congruent with this conclusion: in the former, pathways available for fluid flow consist primarily of microcracks and microporosity. The latter show relatively large subspherical to spherical pores, which could provide relatively less constricted and tortuous pathways for flow. By extension, rocks in the field should largely follow one power-law trend below a porosity around 14–16% (where fluid flow is crack controlled), and another trend above this threshold (where fluid flow is pore controlled). Fig. 9c shows our field data overlain with a relation derived from all of the compiled Volcán de Colima laboratory data ($x^* = 16.2\%$): it can be seen that despite the scatter observed in the field data—and the attendant issues with compiling laboratory data—the permeability–porosity trend is congruent with a changepoint model. In fact, essentially all of the variability between laboratory measurements is encapsulated by the natural variability observed in the field data. While a discrete changepoint x^* is probably an over-simplification of the transition from a low to a high exponent (and vice versa), these data strongly suggest that this model captures a significant component of the microstructural complexity displayed by edifice-forming volcanic rocks. Further, the close agreement between the optimal changepoints determined for our data and compiled data from other authors hints that the changepoint must occur within a relatively small porosity range (i.e. within a few percent of $\varphi = 14\%$).

As discussed by Heap et al. (2014a), the changepoint is likely to represent a critical porosity threshold beneath which fluid transport is dominated by tortuous microcracks. Although the genesis of porosity is initially pre- or syneruptive (i.e. formation porosity), we observe ubiquitous microcracks across the range of collected porosities (i.e. porosity likely formed during emplacement and transport; Fig. 8a, c, d). As a result, the values of permeability measured on edifice-forming rocks are likely to be higher than their pre- or syneruptive permeabilities. In samples with low initial porosity (Fig. 8a–c), fluid flow is restricted largely to these tortuous microcracks. Where the initial porosity is higher (Fig. 8d–f), the cracks serve to link existing porosity. If effective fluid pathways exist, then additional porosity (formed by bubble growth, thermal cracking, or transport processes) has a marginal impact on permeability, explaining why the power-law exponent is lower above the changepoint porosity.

Overall pore connectivity (given by Γ) can be seen to follow two distinct patterns (Fig. 7e) as porosity increases: connectivity increases linearly until the predicted changepoint, after which it plateaus around $\Gamma = 1$. This indicates that any additional porosity below the changepoint serves to connect a correspondingly larger fraction of the pore space. Above around 14% porosity, essentially all porosity is connected to the outside of the sample, and thus constitutes a potential fluid pathway. The permeability is thus little influenced by additional porosity; rather, the effectiveness of pore connections—determined largely by pore apertures—must govern the flow of fluid through the rock.

4. Conclusions

The goal of this combined field and laboratory study was to explore the relationship between porosity and permeability of edifice-forming andesitic rocks at Volcán de Colima, and to identify the likely microstructural controls governing this relationship (given its structural and eruptive characteristics, we assert that Volcán de Colima is typical of many andesitic stratovolcanoes). Our study highlights a wide range of bulk density of samples at Volcán de Colima, suggesting of a wide range of eruptive styles. With increasing distance from the active vent, the measured samples tend towards a skewed density distribution, as dense, low-porosity rocks typically survive comminution during remobilisation more so than less indurate rocks. The measured densities (between 1142.40 and 2813.79 kg m^{-3}) correspond to porosity values between 2.5 and 73%. Measured field permeabilities are in the range of 10^{-16} to 10^{-11} m^2, encompassing values significantly greater than those generally assumed for fluid transport in magma, and thus emphasising the importance of host-rock permeability in facilitating outgassing of volatiles and, in turn, governing eruption dynamics. For any given porosity we observe a permeability range of up to four orders of magnitude, which can be partially explained by natural variability in microstructural attributes (pore geometries and pore connectivity). This range of stochasticity is little affected by meso-scale textural differences, oxidation, or alteration, although the bubble elongation associated with scoracious deposits fosters the largest degree of scatter. In the laboratory, permeabilities as low as 9.5×10^{-17} m^2 were measured, corresponding to low porosities ($\leq 5\%$) and high internal surface areas. Microstructural analysis reveals that high surface areas are associated with an inter-microlite microporosity, which does not appear to significantly increase porosity or pore connectivity, resulting in underestimation of fluid pathway tortuosities. We observe that low porosity samples are dominated by tortuous microcracks, whereas highly-porous samples contain large interconnected pores. Consistently low calculated tortuosity values highlight that the Kozeny–Carman relation is a poor predictor of connectivity and cannot adequately capture the microstructural complexity of volcanic rocks. The ratio of total and unconnected porosity Γ comprises a useful proxy for determining the overall connectivity of a sample, although it does not describe the efficiency of fluid flow through pore networks. The relationship of permeability to connected porosity was observed to follow two distinct power-law trends: a threshold in connected porosity was identified at approximately 14% using piecewise regression and Bayesian Information Criterion analyses. At this changepoint, we assume that the permeable network of these volcanic rocks becomes pore-dominated rather than microcrack-dominated. The changepoint is congruent with a change in the relation between Γ and connected porosity. The improved connectivity of fluid pathways above ~14–16% is manifest in a reduced exponent in the power-law relation between permeability and porosity. While the supposition that this exponent changes at a distinct changepoint is a simplification, we find that it describes well our permeability trend, as well as data from previous studies. A firmer understanding of the microstructural attributes and physical properties controlling permeability is important for the long-term goal of understanding volcanic outgassing and the attendant controls on the frequent transition between effusive and explosive behaviour characteristic of many active andesitic volcanoes.

Acknowledgements

Oliver Lamb, Tom McLaughlin, Graeme Alexander William Sinclair, and Josh Greenwood are thanked for their assistance during the field campaign, and Yan Lavallée and Alex Kushnir for the discussions. The field campaign was funded in part by the framework of the LABEX ANR-11-LABX-0050_G-EAU-THERMIE-PROFONDE and therefore benefits from a funding from the state managed by the French National Research Agency as part of the Investments for the future program. JF acknowledges the Initiative d'Excellence (IDEX) framework of the French State. NV thanks the Universidad de Colima for its assistance via FRABA 2014. Gilles Morvan is thanked for his assistance using the SEM. The field data may be made available on request. We also thank Ulrich Kueppers and an anonymous reviewer, whose comments helped improve and clarify this manuscript.

Appendix A

The field permeameter used in this study was the TinyPerm II, developed by New England Research, Inc. and Vindum Engineering, Inc. The

unit comprises a nozzle and chamber attached to a volume syringe with a plunger. An absolute air pressure transducer is housed near the nozzle, and a volume transducer situated within the syringe. To use the permeameter, the nozzle is pressed against a rock surface, then the plunger is depressed, evacuating air from the sample. The sample at ambient pressure is thus subjected to a pressure profile as air is drawn from the rock; this pressure differential returns to ambient after some time interval, dependent on the permeability of the rock. A microcontroller unit records the absolute pressure at the nozzle-rock interface, while monitoring the internal syringe volume and computing the response function of the pressure transient. The underlying semi-empirical theory is described fully in Brown and Smith (2013). Note that this permeameter uses atmospheric air as a permeant, rather than a truly inert fluid as would be used in laboratory measurements.

The resultant value, here called $\dot{k}$, is displayed onscreen, and corresponds to Darcian permeability such that $\dot{k} = (-0.8206 \log_{10}(k) + 12.8737)$. In order to convert $\dot{k}$ into SI units, we rearrange such that

$$k = \frac{10^{\left(\left(\dot{k} - 12.8737\right)/-0.8206\right)}}{9.869233 \times 10^{10}} \quad \text{(A1)}$$

in m^2.

To test the accuracy and repeatability of the field permeameter, we performed a suite of permeability measurements on sedimentary samples for comparison with laboratory-derived permeability measurements. Blocks of eight sedimentary rocks were cored and a cylindrical sample obtained, nominally 40 mm long and 20 mm in diameter. Gas permeability was measured on these cores using the benchtop steady-state gas permeameter described in the main body of the text. TinyPerm measurements were performed on each of the blocks, parallel to the coring direction. Each block was measured at five or more points, with ten measurements performed at each point. The measured rocks are Bentheim Main (MA) and Basis (BA) sandstone, Bleurswiller sandstone (BWS), Monti Climiti limestone (MCL), Boise sandstone (BO), Darley Dale sandstone (DD), Leitha limestone (L41), and Saint Maximin limestone (SML); physical properties are given in Table A1. These well-studied materials were chosen for this assessment as they exhibit notable homogeneity in their microstructure and pore size distribution; we can thus be confident that a core sample derived from one of these blocks will represent the physical properties of the block as a whole. Notably, the steady-state method yielded results that were consistently within one standard deviation of the mean TinyPerm value. Fig. A1 compares the steady-state permeability measured on cored cylinders with the range of values determined with the TinyPerm unit. When obtaining cores from volcanic rocks that are highly heterogeneous in their pore size distribution, we observe that the measured porosity (and by extension, permeability) can differ from the bulk clast values, as shown in Fig. A2. Notably, despite these differences, the overall permeability–porosity trend, as discussed in the text, remains the same.

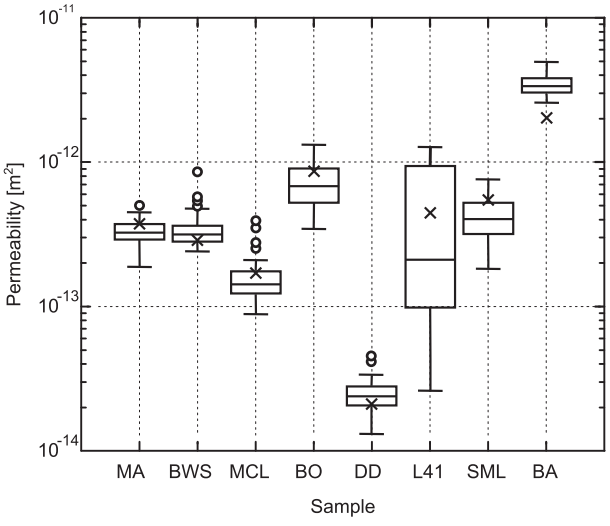

Fig. A1. Box-and-whisker distribution of TinyPerm permeability measurements. Central horizontal line of each box represents the mean measured value. Outliers are shown as circles. Crosses show the results of benchtop steady-state measurements for each sample. The measured rocks were Bentheim Main (MA) and Basis (BA) sandstone, Bleurswiller sandstone (BWS), Monti Climiti limestone (MCL), Boise sandstone (BO), Darley Dale sandstone (DD), Leitha limestone (L41), and Saint Maximin limestone (SML).

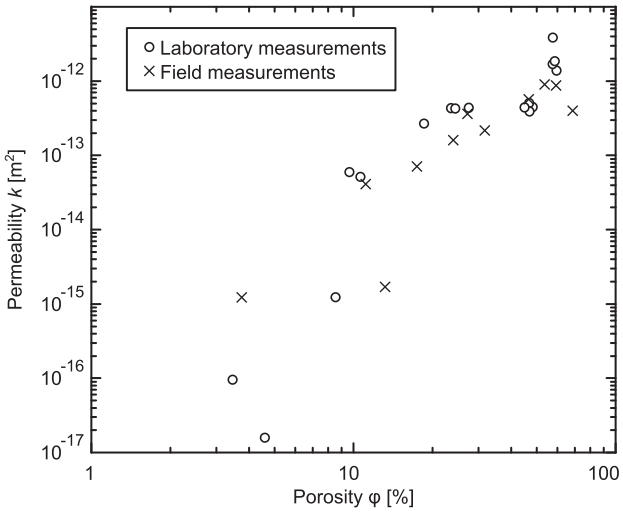

Fig. A2. Comparison of field based whole-clast permeability–porosity measurements and laboratory core measurements.

Repeatability of results from the TinyPerm unit was found to be high, measurements on the same point (i.e. A, B, C, D, E) always being within one order of magnitude, and generally less than 20% either side of mean. Data are given in Table A2.

Two main issues were identified when using the TinyPerm to measure volcanic rock samples. Firstly, obtaining accurate and precise measurements depends on creating an airtight contact between the permeameter nozzle and the sample surface. If the rock surface is non-ideal, then leakage of air into the permeameter chamber can result in over an order of magnitude error in measurements. To preclude this we use a malleable putty on the end of the nozzle (as suggested by the manufacturer) to seal the nozzle to the sample. With sufficient pressure against the sample, use of the putty seal was effective in preventing the premature decay of the pressure gradient. Secondly, the maximum $\dot{k}$ value observable on the microcontroller display is 13, corresponding

Table A1
Laboratory physical property data (porosity and permeability) for cores of selected sedimentary rocks, alongside TinyPerm results from blocks.

Sample	Gas porosity [%]	Gas permeability [m^2]	Mean TinyPerm permeability [m^2]	TinyPerm standard deviation
MA	22.96	3.72×10^{-13}	3.34×10^{-13}	6.65×10^{-14}
BWS	25.78	2.85×10^{-13}	3.47×10^{-13}	1.09×10^{-13}
MCL	28.53	1.70×10^{-13}	1.58×10^{-13}	5.94×10^{-14}
BO	26.00	8.65×10^{-13}	7.26×10^{-13}	2.5×10^{-13}
DD	17.07	2.11×10^{-14}	2.49×10^{-14}	6.78×10^{-15}
L41	24.32	4.47×10^{-13}	5.01×10^{-13}	4.71×10^{-13}
SML	37.82	5.50×10^{-13}	4.26×10^{-13}	1.49×10^{-13}
BA	24.05	4.09×10^{-13}	3.45×10^{-12}	6.02×10^{-13}

Table A2
Full table of (transformed) results from permeability measurements on sedimentary blocks. A, B, C, D, and E represent five randomly selected points on the surface of each block, whereat ten repeat measurements were made.

	Sample							
Measurement	MCL	DD	SML	L41	MA	BA	BWS	BO
A1	1.05×10^{-13}	4.53×10^{-14}	4.04×10^{-13}	7.72×10^{-14}	2.58×10^{-13}	3.71×10^{-12}	3.14×10^{-13}	6.89×10^{-13}
A2	1.35×10^{-13}	4.16×10^{-14}	3.93×10^{-13}	1.84×10^{-13}	4.28×10^{-13}	3.82×10^{-12}	3.14×10^{-13}	7.71×10^{-13}
A3	1.32×10^{-13}	3.33×10^{-14}	5.2×10^{-13}	2.06×10^{-13}	3.05×10^{-13}	3.92×10^{-12}	2.73×10^{-13}	7.71×10^{-13}
A4	1.18×10^{-13}	2.81×10^{-14}	2.81×10^{-13}	1.47×10^{-13}	3.14×10^{-13}	3.82×10^{-12}	2.73×10^{-13}	8.38×10^{-13}
A5	1.43×10^{-13}	3.06×10^{-14}	4.16×10^{-13}	2.81×10^{-13}	2.73×10^{-13}	4.27×10^{-12}	2.81×10^{-13}	8.87×10^{-13}
A6	1.24×10^{-13}	2.44×10^{-14}	4.04×10^{-13}	2.97×10^{-13}	3.61×10^{-13}	2.58×10^{-12}	2.89×10^{-13}	9.12×10^{-13}
A7	1.32×10^{-13}	3.06×10^{-14}	3.32×10^{-13}	2.81×10^{-13}	3.23×10^{-13}	2.65×10^{-12}	2.65×10^{-13}	5.99×10^{-13}
A8	1.32×10^{-13}	2.89×10^{-14}	4.52×10^{-13}	1.9×10^{-13}	3.82×10^{-13}	2.96×10^{-12}	2.44×10^{-13}	5.5×10^{-13}
A9	1.65×10^{-13}	2.58×10^{-14}	3.93×10^{-13}	2.51×10^{-13}	4.04×10^{-13}	2.88×10^{-12}	2.81×10^{-13}	7.09×10^{-13}
A10	2.51×10^{-13}	4.53×10^{-14}	4.52×10^{-13}	2.18×10^{-13}	3.93×10^{-13}	2.96×10^{-12}	3.14×10^{-13}	6.33×10^{-13}
B1	1.24×10^{-13}	2.06×10^{-14}	3.82×10^{-13}	2.58×10^{-14}	2.89×10^{-13}	4.91×10^{-12}	3.14×10^{-13}	7.49×10^{-13}
B2	3.93×10^{-13}	1.47×10^{-14}	4.52×10^{-13}	4.28×10^{-14}	2.89×10^{-13}	4.04×10^{-12}	2.97×10^{-13}	6.7×10^{-13}
B3	1.43×10^{-13}	1.9×10^{-14}	5.2×10^{-13}	3.15×10^{-14}	3.72×10^{-13}	4.51×10^{-12}	2.89×10^{-13}	8.87×10^{-13}
B4	2.06×10^{-13}	2.44×10^{-14}	3.05×10^{-13}	5.21×10^{-14}	3.14×10^{-13}	4.51×10^{-12}	2.81×10^{-13}	9.38×10^{-13}
B5	1.79×10^{-13}	2.18×10^{-14}	3.32×10^{-13}	5.83×10^{-14}	3.32×10^{-13}	4.78×10^{-12}	2.73×10^{-13}	6.89×10^{-13}
B6	1.6×10^{-13}	2.25×10^{-14}	3.72×10^{-13}	1.95×10^{-13}	2.89×10^{-13}	3.82×10^{-12}	2.37×10^{-13}	7.71×10^{-13}
B7	1.95×10^{-13}	1.95×10^{-14}	3.14×10^{-13}	8.88×10^{-14}	3.05×10^{-13}	3.82×10^{-12}	2.73×10^{-13}	7.09×10^{-13}
B8	1.9×10^{-13}	1.9×10^{-14}	3.23×10^{-13}	5.67×10^{-14}	3.23×10^{-13}	3.92×10^{-12}	2.81×10^{-13}	8.62×10^{-13}
B9	1.79×10^{-13}	1.9×10^{-14}	3.42×10^{-13}	5.21×10^{-14}	3.05×10^{-13}	4.04×10^{-12}	2.65×10^{-13}	9.38×10^{-13}
B10	1.74×10^{-13}	1.85×10^{-14}	3.93×10^{-13}	5.67×10^{-14}	2.97×10^{-13}	4.78×10^{-12}	2.89×10^{-13}	8.38×10^{-13}
C1	1.05×10^{-13}	1.32×10^{-14}	2.31×10^{-13}	1.11×10^{-12}	2.97×10^{-13}	3.71×10^{-12}	3.32×10^{-13}	3.93×10^{-13}
C2	1.74×10^{-13}	1.7×10^{-14}	3.05×10^{-13}	1.28×10^{-12}	3.72×10^{-13}	2.96×10^{-12}	3.23×10^{-13}	3.51×10^{-13}
C3	1.74×10^{-13}	2.12×10^{-14}	3.23×10^{-13}	1.28×10^{-12}	4.4×10^{-13}	2.96×10^{-12}	3.32×10^{-13}	3.82×10^{-13}
C4	1.35×10^{-13}	2.18×10^{-14}	3.05×10^{-13}	1.28×10^{-12}	3.32×10^{-13}	3.51×10^{-12}	2.51×10^{-13}	3.42×10^{-13}
C5	1.08×10^{-13}	2.58×10^{-14}	2.81×10^{-13}	1.02×10^{-12}	2.97×10^{-13}	3.41×10^{-12}	3.61×10^{-13}	3.82×10^{-13}
C6	1.32×10^{-13}	$2.44 \times 10_{-14}$	1.79×10^{-13}	9.38×10^{-13}	2.65×10^{-13}	3.13×10^{-12}	3.72×10^{-13}	4.16×10^{-13}
C7	1.43×10^{-13}	2.18×10^{-14}	2.24×10^{-13}	1.21×10^{-12}	3.42×10^{-13}	3.71×10^{-12}	8.62×10^{-13}	4.04×10^{-13}
C8	2.73×10^{-13}	2.01×10^{-14}	2.31×10^{-13}	1.21×10^{-12}	3.51×10^{-13}	2.65×10^{-12}	3.32×10^{-13}	4.78×10^{-13}
C9	1.32×10^{-13}	2.18×10^{-14}	3.32×10^{-13}	1.14×10^{-12}	4.4×10^{-13}	2.58×10^{-12}	3.61×10^{-13}	4.28×10^{-13}
C10	1.05×10^{-13}	2.01×10^{-14}	5.66×10^{-13}	1.17×10^{-12}	3.61×10^{-13}	3.22×10^{-12}	3.51×10^{-13}	4.28×10^{-13}
D1	1.47×10^{-13}	2.73×10^{-14}	5.99×10^{-13}	1.08×10^{-13}	3.72×10^{-13}	3.32×10^{-12}	5.66×10^{-13}	1.14×10^{-12}
D2	1.02×10^{-13}	2.31×10^{-14}	6.51×10^{-13}	1.18×10^{-13}	4.16×10^{-13}	3.13×10^{-12}	5.35×10^{-13}	1.08×10^{-12}
D3	1.39×10^{-13}	2.89×10^{-14}	5.5×10^{-13}	1.35×10^{-13}	4.28×10^{-13}	3.82×10^{-12}	4.4×10^{-13}	1.31×10^{-12}
D4	1.24×10^{-13}	3.33×10^{-14}	6.16×10^{-13}	5.67×10^{-14}	5.06×10^{-13}	3.13×10^{-12}	4.78×10^{-13}	1.11×10^{-12}
D5	1.35×10^{-13}	2.81×10^{-14}	7.49×10^{-13}	1.51×10^{-13}	4.28×10^{-13}	3.22×10^{-12}	4.92×10^{-13}	1.08×10^{-12}
D6	1.32×10^{-13}	1.7×10^{-14}	7.09×10^{-13}	9.94×10^{-14}	3.72×10^{-13}	2.8×10^{-12}	4.92×10^{-13}	1.14×10^{-12}
D7	1.56×10^{-13}	2.38×10^{-14}	7.09×10^{-13}	1.18×10^{-13}	3.93×10^{-13}	2.65×10^{-12}	5.35×10^{-13}	1.11×10^{-12}
D8	1.14×10^{-13}	3.06×10^{-14}	7.29×10^{-13}	1.74×10^{-13}	3.32×10^{-13}	2.96×10^{-12}	2.97×10^{-13}	1.02×10^{-12}
D9	1.84×10^{-13}	3.15×10^{-14}	7.09×10^{-13}	6.9×10^{-14}	3.51×10^{-13}	3.13×10^{-12}	4.04×10^{-13}	1.14×10^{-12}
D10	1.69×10^{-13}	1.85×10^{-14}	5.82×10^{-13}	1.84×10^{-13}	4.4×10^{-13}	3.41×10^{-12}	4.16×10^{-13}	9.92×10^{-13}
E1	8.88×10^{-14}	2.31×10^{-14}	5.5×10^{-13}	1.02×10^{-12}	1.84×10^{-13}	3.82×10^{-12}	3.14×10^{-13}	5.2×10^{-13}
E2	2.58×10^{-13}	2.44×10^{-14}	2.44×10^{-13}	9.65×10^{-13}	2.44×10^{-13}	2.96×10^{-12}	2.81×10^{-13}	5.35×10^{-13}
E3	9.94×10^{-14}	2.06×10^{-14}	2.97×10^{-13}	8.87×10^{-13}	2.97×10^{-13}	2.88×10^{-12}	2.97×10^{-13}	5.06×10^{-13}
E4	1.43×10^{-13}	2.81×10^{-14}	2.12×10^{-13}	9.38×10^{-13}	2.51×10^{-13}	3.13×10^{-12}	3.42×10^{-13}	5.66×10^{-13}
E5	9.94×10^{-14}	3.06×10^{-14}	3.72×10^{-13}	1.08×10^{-12}	2.31×10^{-13}	3.61×10^{-12}	3.14×10^{-13}	5.06×10^{-13}
E6	1.51×10^{-13}	2.06×10^{-14}	4.52×10^{-13}	8.38×10^{-13}	2.81×10^{-13}	3.22×10^{-12}	3.23×10^{-13}	5.82×10^{-13}
E7	1.56×10^{-13}	2.51×10^{-14}	4.78×10^{-13}	9.38×10^{-13}	2.18×10^{-13}	3.32×10^{-12}	3.72×10^{-13}	6.16×10^{-13}
E8	1.21×10^{-13}	2.31×10^{-14}	4.16×10^{-13}	8.62×10^{-13}	2.73×10^{-13}	3.22×10^{-12}	3.51×10^{-13}	6.51×10^{-13}
E9	1.56×10^{-13}	2.38×10^{-14}	4.4×10^{-13}	9.38×10^{-13}	3.05×10^{-13}	3.13×10^{-12}	2.89×10^{-13}	6.16×10^{-13}
E10	3.51×10^{-13}	2.51×10^{-14}	4.65×10^{-13}	9.38×10^{-13}	3.42×10^{-13}	2.96×10^{-12}	3.05×10^{-13}	6.7×10^{-13}

to a k of 6.92×10^{-16} m^2. Any and all samples with a permeability $\leq 6.92 \times 10^{-16}$ m^2 are thus indistinguishable; accordingly, a $\dot{k}$ value of 12.99 has been implemented as the limit in our study.

Appendix B

Fig. B1 shows the densities yielded by two methods performed on the sample suite at the Experimental Geophysics laboratory, Strasbourg. The double-weight method is equivalent to that carried out in the field; the second method comprises the volumetric mass density determined by the ratio of the geometric volume and dry mass of a cylindrical sample. As evidenced in Fig. B1, the double-weight values are progressively higher than the geometric values at decreasing densities (i.e. higher porosities). This is a function of the capacity for water imbibition through surface pores over the timescale of each measurement (typically about 5 s); incorporating the parameters of the fitted line into further analyses of density data allows this deviation to be accounted for. Porosity is a direct function of the ratio of bulk and particle densities: the relationship between porosity and volumetric mass density can thus be well constrained, as in Fig. B1b, where the inverse of the absolute value of the slope corresponds to the particle density. The strong linear correlation between these values attests to a relative lack of variation in bulk composition and thus particle density between samples. The correlations described by Fig. B1a and B1b have been encompassed in an empirical relation (Fig. B1c), subsequently used to estimate connected porosity from the initial field density data.

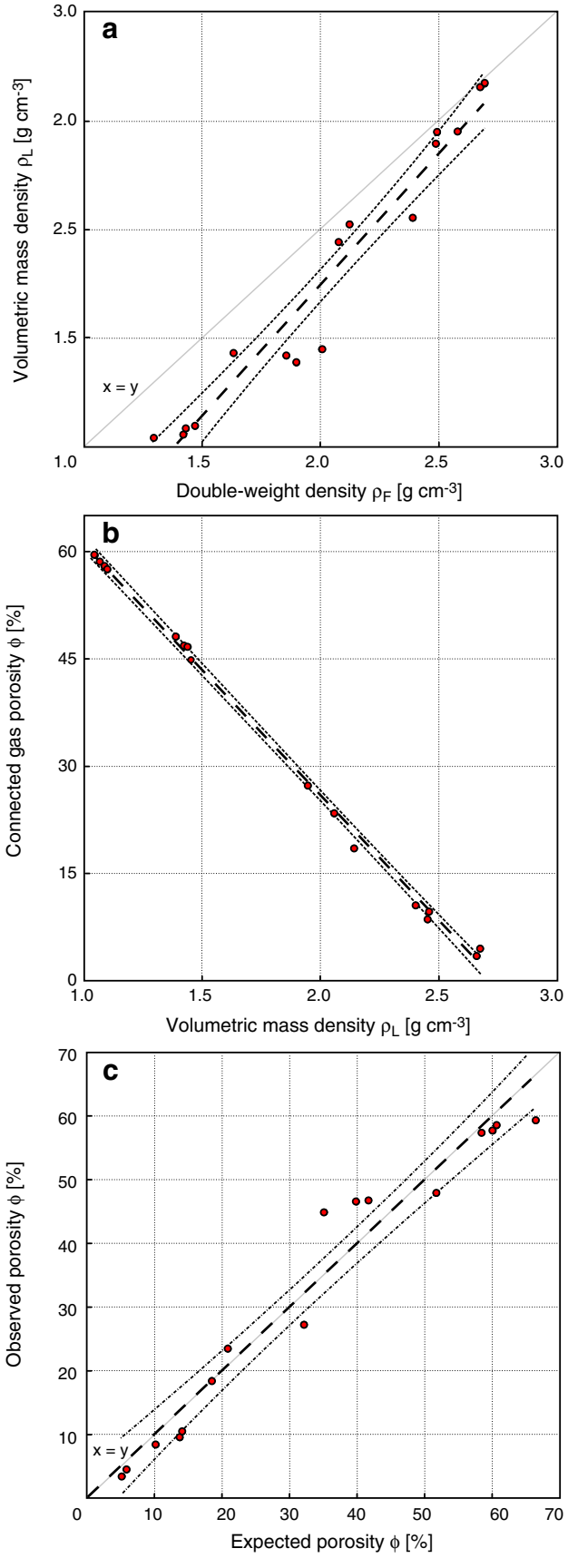

References

Bernabé, Y., Mok, U., Evans, B., 2003. Permeability–porosity relationships in rocks subjected to various evolution processes. Pure Appl. Geophys. 160 (5-6), 937–960.

Bernabé, Y., Li, M., Maineult, A., 2010. Permeability and pore connectivity: a new model based on network simulations. J. Geophys. Res. 155, B10203. http://dx.doi.org/10.1023/2010JB007444.

Bernard, B., Kueppers, U., Ortiz, H., 2015. Revisiting the statistical analysis of pyroclast density and porosity data. Solid Earth Discuss. 7, 1077–1095. http://dx.doi.org/10.5194/sed-7-1077-2015 (2015).

Bernard, M.L., Zamora, M., Géraud, Y., Boudon, G., 2007. Transport properties of pyroclastic rocks from Montagne Pelée volcano (Martinique, Lesser Antilles). Journal of Geophysical Research: Solid Earth (1978–2012) 112 (B5). http://dx.doi.org/10.1029/2006JB004385.

Biggs, J., Mothes, P., Ruiz, M., Amelung, F., Dixon, T.H., Baker, S., Hong, S.H., 2010. Stratovolcano growth by co-eruptive intrusion: the 2008 eruption of Tungurahua Ecuador. Geophys. Res. Lett. 37 (21). http://dx.doi.org/10.1029/2010GL044942.

Blower, J., 2001. Factors controlling permeability–porosity relationships in magma. Bull. Volcanol. 63 (7), 497–504. http://dx.doi.org/10.1007/s004450100172.

Bourbie, T., Zinszner, B., 1985. Hydraulic and acoustic properties as a function of porosity in Fontainebleau sandstone. J. Geophys. Res. Solid Earth (1978–2012) 90 (B13), 11524–11532. http://dx.doi.org/10.1029/JB090iB13p11524.

Bretón-González, M., Ramírez, J.J., Navarro, C., 2002. Summary of the historical eruptive activity of Volcán De Colima, Mexico 1519–2000. J. Volcanol. Geotherm. Res. 117 (1-2), 21–46. http://dx.doi.org/10.1016/S0377-0273(02)00233-0.

Brown, S., Smith, M., 2013. A transient-flow syringe air permeameter. Geophysics 78 (5), D307–D313. http://dx.doi.org/10.1190/geo2012-0534.1.

Camus, G., Gourgaud, A., Mossand-Berthommier, P.C., Vincent, P.M., 2000. Merapi (Central Java, Indonesia): an outline of the structural and magmatological evolution, with a special emphasis to the major pyroclastic events. J. Volcanol. Geotherm. Res. 100 (1), 139–163. http://dx.doi.org/10.1016/S0377-0273(00)00135-9.

Carman, P.C., 1937. Fluid flow through granular beds. Trans. Inst. Chem. Eng. 15, 150–166.

Carrasco-Núñez, G., 2000. Structure and proximal stratigraphy of Citlaltepetl volcano (Pica de Orizaba), Mexico. Cenozoic Tectonics Volcan. Mex. 334, 247. http://dx.doi.org/10.1130/0-8137-2334-5.247.

Cashman, K.V., Mangan, M.T., Newman, S., 1994. Surface degassing and modifications to vesicle size distributions in active basalt flows. J. Volcanol. Geotherm. Res. 61 (1), 45–68. http://dx.doi.org/10.1016/0377-0273(94)00015-8.

Castro, J.M., Bindeman, I.N., Tuffen, H., Schipper, C.I., 2014. Explosive origin of silicic lava: textural and δD–H_2O evidence for pyroclastic degassing during rhyolite effusion. Earth Planet. Sci. Lett. 405, 52–61. http://dx.doi.org/10.1016/j.epsl.2014.08.012.

Clarke, A.B., Neri, A., Voight, B., Macedonio, G., Druitt, T.H., 2002a. Computational modelling of the transient dynamics of the August 1997 Vulcanian explosions at Soufriere Hills Volcano, Montserrat: influence of initial conduit conditions on near-vent pyroclastic dispersal. Geol. Soc. Lond. Mem. 21, 319–348.

Clarke, A.B., Voight, B., Neri, A., Macedonio, G., 2002b. Transient dynamics of vulcanian explosions and column collapse. Nature 415 (6874), 897–901. http://dx.doi.org/10.1038/415897a.

Clavaud, J.B., Maineult, A., Zamora, M., Rasolofosaon, P., Schlitter, C., 2008. Permeability anisotropy and its relations with porous medium structure. J. Geophys. Res. Solid Earth (1978–2012) 113 (B1). http://dx.doi.org/10.1029/2007JB005004.

Collinson, A.S.D., Neuberg, J.W., 2012. Gas storage, transport and pressure changes in an evolving permeable volcanic edifice. J. Volcanol. Geotherm. Res. 243, 1–13. http://dx.doi.org/10.1016/j.jvolgeores.2012.06.027.

Costa, A., 2006. Permeability–porosity relationship: a reexamination of the Kozeny–Carman equation based on a fractal pore-space geometry assumption. Geophys. Res. Lett. 33 (2). http://dx.doi.org/10.1029/2005GL025134.

Day, S.J., 1996. Hydrothermal pore fluid and the stability of porous, permeable volcanoes. Q. J. Geol. Soc. Lond. 111, 77–93. http://dx.doi.org/10.1144/GSL.SP.1996.110.01.06.

De Maisonneuve, C.B., Bachmann, O., Burgisser, A., 2009. Characterization of juvenile pyroclasts from the Kos Plateau Tuff (Aegean Arc): insights into the eruptive dynamics of a large rhyolitic eruption. Bulletin of volcanology 71 (6), 643–658. http://dx.doi.org/10.1007/s00445-008-0250-x.

Degruyter, W., Bachmann, O., Burgisser, A., 2010. Controls on magma permeability in the volcanic conduit during the climactic phase of the Kos Plateau Tuff eruption (Aegean Arc). Bulletin of Volcanology 72 (1), 63–74. http://dx.doi.org/10.1007/s00445-009-0302-x.

Edmonds, M., Oppenheimer, C., Pyle, D.M., Herd, R.A., Thompson, G., 2003. SO2 emissions from Soufrière Hills Volcano and their relationship to conduit permeability,

Fig. B1. (a) gives a comparison between density values yielded by the double-weight (field) method ρ_F and the volumetric mass (laboratory) method ρ_L. The deviation from $x = y$ can be described empirically such that $\rho_L = m_A\rho_F + c_A$, [$R^2 = 0.95$]. Thin dashed lines represent the upper and lower 95% confidence intervals (CI) around the fit line (thick dashed line). In (b), connected gas porosity φ as measured by helium pycnometry is shown against volumetric mass density for andesite cores. The relationship is of the form $\varphi = m_B\,\rho_L + c_B$, [$R^2 = 1.00$]. Thin dashed lines represent the upper and lower 95% confidence intervals (CI) around the fit line (thick dashed line). (c) shows the results of semi-empirical transformation of double-weight core density measurements (Expected) against measured gas porosity (Observed) described by the dashed line [$R^2 = 0.99$]. Transformation is of the form $\varphi = \alpha[m_B(m_A\rho_L + c_A) + c_B]$, where m_A, c_A, m_B and, c_B are fit components from (a) and (b). The coefficient α is an empirical constant close to 1. Grey line describes Observed = Expected porosity. (For interpretation of the references to colour in this figure legend, the reader is referred to the web version of this article.)

hydrothermal interaction and outgassing regime. J. Volcanol. Geotherm. Res. 124, 23–43. http://dx.doi.org/10.1016/S0377-0273(03)00041-6.
Eichelberger, J.C., Carrigan, C.R., Westrich, H.R., Price, R.H., 1986. Non-explosive silicic volcanism. Nature 323 (6089), 598–602. http://dx.doi.org/10.1038/323598a0.
Gamble, J.A., Wood, C.P., Price, R.C., Smith, I.E.M., Stewart, R.B., Waight, T., 1999. A fifty year perspective of magmatic evolution on Ruapehu Volcano, New Zealand: verification of open system behaviour in an arc volcano. Earth Planet. Sci. Lett. 170 (3), 301–314. http://dx.doi.org/10.1016/S0012-821X(99)00106-5.
Gardeweg, M.C., Sparks, R.S.J., Matthews, S.J., 1998. Evolution of Lascar volcano, northern Chile. J. Geol. Soc. 155 (1), 89–104. http://dx.doi.org/10.1144/gsjgs.155.1.0089.
Gaunt, H.E., Sammonds, P.R., Meredith, P.G., Smith, R., Pallister, J.S., 2014. Pathways for degassing during the lava dome eruption of Mount St. Helens 2004–2008. Geology 42 (11), 947–950. http://dx.doi.org/10.1130/G35940.1.
Gaylord, D.R., Neall, V.E., 2012. Subedifice collapse of an andesitic stratovolcano: the Maitahi Formation, Taranaki Peninsula, New Zealand. Geol. Soc. Am. Bull. 124 (1-2), 181–199. http://dx.doi.org/10.1130/B30141.1.
Gonnermann, H.M., Manga, M., 2003. Explosive volcanism may not be an inevitable consequence of magma fragmentation. Nature 426 (6965), 432–435. http://dx.doi.org/10.1038/nature02138.
Gonnermann, H.M., Manga, M., 2007. The fluid mechanics inside a volcano. Annu. Rev. Fluid Mech. 39, 321–356. http://dx.doi.org/10.1146/annurev.fluid.39.050905.110207.
Gudmundsson, A., 2012. Magma chambers: formation, local stresses, excess pressures, and compartments. J. Volcanol. Geotherm. Res. 237, 19–41. http://dx.doi.org/10.1016/j.jvolgeores.2012.05.015.
Guéguen, Y., Palciauskas, V., 1994. Introduction to the Physics of Rocks. Princeton University Press, UK.
Hatton, C.G., Main, I.G., Meredith, P.G., 1994. Non-universal scaling of fracture length and opening displacement. Nature 367 (6459), 160–162. http://dx.doi.org/10.1038/367160a0.
Heap, M.J., Lavallée, Y., Petrakova, L., Baud, P., Reuschlé, T., Varley, N.R., Dingwell, D.B., 2014a. Microstructural controls on the physical and mechanical properties of edifice-forming andesites at Volcán de Colima, Mexico. J. Geophys. Res. Solid Earth 119. http://dx.doi.org/10.1002/2013JB010521.
Heap, M.J., Kolzenburg, S., Russell, J.K., Campbell, M.E., Welles, J., Farquharson, J.I., Ryan, A., 2014b. Conditions and timescales for welding block-and-ash flow deposits. J. Volcanol. Geotherm. Res. 289, 202–209. http://dx.doi.org/10.1016/j.jvolgeores.2014.11.010.
Heap, M.J., Farquharson, Y., Baud, P., Lavallée, Y., Reuschlé, T., 2015. Fracture and compaction of andesite in a volcanic edifice. Bull. Volcanol. (submitted for publication).
Houghton, B.F., Latter, J.H., Hackett, W.R., 1987. Volcanic hazard assessment for Ruapehu composite volcano, Taupo volcanic zone, New Zealand. Bull. Volcanol. 49 (6), 737–751. http://dx.doi.org/10.1007/BF01079825.
Invernizzi, C., Pierantoni, P.P., Chiodi, A., Maffucci, R., Corrado, S., Baez, W., Viramonte, J., 2014. Preliminary assessment of the geothermal potential of Rosario de la Frontera area (Salta, NW Argentina): insight from hydro-geological, hydro-geochemical and structural investigations. J. S. Am. Earth Sci. 54, 20–36. http://dx.doi.org/10.1016/j.jsames.2014.04.003.
James, M.R., Varley, N., 2012. Identification of structural controls in an active lava dome with high resolution DEMs: Volcán de Colima, Mexico. Geophys. Res. Lett. 39, L22303. http://dx.doi.org/10.1029/2012GL054245.
Jaupart, C., 1998. Gas loss from magmas through conduit walls during eruption. J. Geol. Soc. 145, 73–90. http://dx.doi.org/10.1144/GSL.SP.1996.145.01.05.
John, D.A., Sisson, T.W., Breit, G.N., Rye, R.O., Vallance, J.W., 2008. Characteristics, extent and origin of hydrothermal alteration at Mount Rainier Volcano, Cascades Arc, USA: implications for debris-flow hazards and mineral deposits. J. Volcanol. Geotherm. Res. 175 (3), 289–314. http://dx.doi.org/10.1016/j.jvolgeores.2008.04.004.
Kendrick, J.E., Lavallée, Y., Hess, K.U., Heap, M.J., Gaunt, H.E., Meredith, P.G., Dingwell, D.B., 2013. Tracking the permeable porous network during strain-dependent magmatic flow. J. Volcanol. Geotherm. Res. 260, 117–126. http://dx.doi.org/10.1016/j.jvolgeores.2013.05.012.
Klug, C., Cashman, K.V., 1996. Permeability development in vesiculating magmas: implications for fragmentation. Bull. Volcanol. 58 (2-3), 87–100. http://dx.doi.org/10.1007/s00445005012.
Klug, C., Cashman, K., Bacon, C., 2002. Structure and physical characteristics of pumice from the climactic eruption of Mount Mazama (Crater Lake). Or. Bull. Volcanol. 64 (7), 486–501. http://dx.doi.org/10.1007/s00445-002-0230-5.
Kolzenburg, S., Heap, M.J., Lavallée, Y., Russell, J.K., Meredith, P.G., Dingwell, D.B., 2012. Strength and permeability recovery of tuffisite-bearing andesite. Solid Earth 3 (2), 191–198. http://dx.doi.org/10.5194/se-3-191-2012.
Kozeny, J., 1927. Über kapillare Leitung des Wassers im Boden:(Aufstieg, Versickerung und Anwendung auf die Bewässerung). Hölder-Pichler-Tempsky.
Kueppers, U., Scheu, B., Spieler, O., Dingwell, D.B., 2005. Field-based density measurements as tool to identify preeruption dome structure: set-up and first results from Unzen volcano, Japan. J. Volcanol. Geotherm. Res. 141 (1), 65–75. http://dx.doi.org/10.1016/j.jvolgeores.2004.09.005.
Kueppers, U., Putz, C., Spieler, O., Dingwell, D.B., 2012. Abrasion in pyroclastic density currents: insights from tumbling experiments. Phys. Chem. Earth A B C 45, 33–39. http://dx.doi.org/10.1016/j.pce.2011.09.002.
Lacey, A., Ockendon, J.R., Turcotte, D.L., 1981. On the geometrical form of volcanoes. Earth Planet. Sci. Lett. 54 (1), 139–143. http://dx.doi.org/10.1016/0012-821X(81)90074-1.
Lavallée, Y., Varley, N.R., Alatorre-Ibargüengoitia, M.A., Hess, K.U., Kueppers, U., Mueller, S., Richard, D., Scheu, B., Spieler, O., Dingwell, D.B., 2012. Magmatic architecture of dome building eruptions at Volcán de Colima, Mexico. Bull. Volcanol. 74, 249–260. http://dx.doi.org/10.1007/s00445-011-0518-4.
Lavallée, Y., Benson, P.M., Heap, M.J., Hess, K.U., Flaws, A., Schillinger, B., Dingwell, D.B., 2013. Reconstructing magma failure and the degassing network of dome-building eruptions. Geology 41 (4), 515–518. http://dx.doi.org/10.1130/G33948.1.
Lev, E., Spiegelman, M., Wysocki, R.J., Karson, J.A., 2012. Investigating lava flow rheology using video analysis and numerical flow models. J. Volcanol. Geotherm. Res. 247–248, 62–73. http://dx.doi.org/10.1016/j.jvolgeores.2012.08.002.
Luhr, J.F., 2002. Petrology and geochemistry of the 1991 and 1998–1999 lava flows from Volcán de Colima, México: implications for the end of the current eruptive cycle. J. Volcanol. Geotherm. Res. 117, 169–194. http://dx.doi.org/10.1016/S0377-0273(02)00243-3.
Main, I.G., Leonard, T., Papasouliotis, O., Hatton, C.G., Meredith, P.G., 1999. One slope or two? Detecting statistically significant breaks of slope in geophysical data, with application to fracture scaling relationships. Geophys. Res. Lett. 26 (18), 2801–2804. http://dx.doi.org/10.1029/1999GL005372.
Manga, M., Patel, A., Dufek, J., 2011. Rounding of pumice clasts during transport: field measurements and laboratory studies. Bull. Volcanol. 73 (3), 321–333. http://dx.doi.org/10.1007/s00445-010-0411-6.
Melnik, O., Sparks, R.S.J., 2002. Dynamics of magma ascent and lava extrusion at Soufrière Hills Volcano, Montserrat. J. Geol. Soc. Lond. Mem. 21 (1), 153–171. http://dx.doi.org/10.1144/GSL.MEM.2002.021.01.07.
Mora, J.C., Macıas, J.L., Saucedo, R., Orlando, A., Manetti, P., Vaselli, O., 2002. Petrology of the 1998–2000 products of Volcán de Colima, México. J. Volcanol. Geotherm. Res. 117 (1), 195–212. http://dx.doi.org/10.1016/S0377-0273(02)00244-5.
Mueller, S.P., 2006. Permeability and porosity as constraints on the explosive eruption of magma: laboratory experiments and field investigations. (PhD Thesis). University of Munich, Munich, Germany.
Mueller, S., Melnik, O., Spieler, O., Scheu, B., Dingwell, D.B., 2005. Permeability and degassing of dome lavas undergoing rapid decompression: an experimental determination. Bull. Volcanol. 67 (6), 526–538. http://dx.doi.org/10.1007/s00445-004-0392-4.
Mueller, S., Scheu, B., Kueppers, U., Spieler, O., Richard, D., Dingwell, D.B., 2011. The porosity of pyroclasts as an indicator of volcanic explosivity. J. Volcanol. Geotherm. Res. 203 (3), 168–174. http://dx.doi.org/10.1016/j.jvolgeores.2011.04.006.
Norini, G., Capra, L., Groppelli, G., Agliardi, F., Pola, A., Cortes, A., 2010. Structural architecture of the Colima Volcanic Complex. J. Geophys. Res. Solid Earth (1978–2012) 115 (B12). http://dx.doi.org/10.1029/2010JB007649.
Okumura, S., Sasaki, O., 2014. Permeability reduction of fractured rhyolite in volcanic conduits and its control on eruption cyclicity. Geology 42 (10), 843–846. http://dx.doi.org/10.1130/G35855.1.
Plail, M., Edmonds, M., Humphreys, M., Barclay, J., Herd, R.A., 2014. Geochemical evidence for relict degassing pathways preserved in andesite. Earth Planet. Sci. Lett. 386, 21–33. http://dx.doi.org/10.1016/j.epsl.2013.10.044.
Possemiers, M., Huysmans, M., Peeters, L., Batelaan, O., Dassargues, A., 2012. Relationship between sedimentary features and permeability at different scales in the Brussels Sands. Geol. Belg. 15 (3).
Rabbani, A., Jamshidi, S., 2014. Specific surface and porosity relationship for sandstones for prediction of permeability. Int. J. Rock Mech. Min. Sci. 71, 25–32. http://dx.doi.org/10.1016/j.ijrmms.2014.06.013.
Reid, M.E., 2004. Massive collapse of volcano edifices triggered by hydrothermal pressurization. Geology 32 (5), 373–376. http://dx.doi.org/10.1130/G20300.1.
Reubi, O., Blundy, J., 2008. Assimilation of plutonic roots, formation of high-K 'exotic' melt inclusions and genesis of andesitic magmas at Volcán de Colima, Mexico. J. Petrol. 49 (12), 2221–2243. http://dx.doi.org/10.1093/petrology/egn066.
Richard, D., Scheu, B., Mueller, S.P., Spieler, O., Dingwell, D.B., 2013. Outgassing: influence on speed of magma fragmentation. J. Geophys. Res. Solid Earth 118, 862–877. http://dx.doi.org/10.1002/jgrb.50080.
Robin, C., Camus, G., Gourgaud, A., 1991. Eruptive and magmatic cycles at Fuego de Colima volcano (Mexico). J. Volcanol. Geotherm. Res. 45 (3), 209–225. http://dx.doi.org/10.1016/0377-0273(91)90060-D.
Rodríguez-Elizarrarás, S.R., 1995. Estratigrafía y estructura del Volcán de Colima, México. Rev. Mex. Cienc. Geol. 12, 22–46.
Rose Jr., W.I., Grant, N.K., Hahn, G.A., Lange, I.M., Powell, J.L., Easter, J., Degraff, J.M., 1977. The evolution of Santa Maria volcano, Guatemala. J. Geol. 63–87.
Saar, M.O., Manga, M., 1999. Permeability-porosity relationship in vesicular basalts. Geophys. Res. Lett. 26 (1), 111–114. http://dx.doi.org/10.1029/1998GL900256.
Sahimi, M., 1994. Applications of Percolation Theory. Taylor Francis, London, UK.
Savov, I.P., Luhr, J.F., Navarro-Ochoa, C., 2008. Petrology and geochemistry of lava and ash erupted from Volcán Colima, Mexico, during 1998–2005. J. Volcanol. Geotherm. Res. 174, 241–256. http://dx.doi.org/10.1016/j.jvolgeores.2008.02.007.
Shields, J.K., Mader, H.M., Pistone, M., Caricchi, L., Floess, D., Putlitz, B., 2014. Strain-induced outgassing of three-phase magmas during simple shear. J. Geophys. Res. Solid Earth 119 (9), 6936–6957. http://dx.doi.org/10.1002/2014JB011111.
Smyth, H., Hall, R., Hamilton, J., Kinny, P., 2005. East Java: Cenozoic basins, volcanoes and ancient basement. Indonesian Petroleum Association, Proceedings 30th Annual Convention, pp. 251–266.
Sruoga, P., Rubinstein, N., Hinterwimmer, G., 2004. Porosity and permeability in volcanic rocks: a case study on the Serie Tobífera, South Patagonia, Argentina. J. Volcanol. Geotherm. Res. 132 (1), 31–43. http://dx.doi.org/10.1016/S0377-0273(03)00419-0.
Taisne, B., Jaupart, C., 2008. Magma degassing and intermittent lava dome growth. Geophys. Res. Lett. 35 (20). http://dx.doi.org/10.1029/2008GL035432.
Tait, S., Thomas, R., Gardner, J., Jaupart, C., 1998. Constraints on cooling rates and permeabilities of pumice in an explosive eruption jet from colour and magnetic mineralogy. J. Volcanol. Geotherm. Res. 86 (1), 79–91. http://dx.doi.org/10.1016/S0377-0273(98)00075-4.
Valdez-Moreno, G., Schaaf, P., Macías, J.L., Kusakabe, M., 2006. New Sr–Nd–Pb–O isotope data for Colima volcano and evidence for the nature of the local basement. Geol. Soc. Am. Spec. Pap. 402, 45–63.

Varley, N.R., Taran, Y., 2003. Degassing processes of Popocatépetl and Volcán de Colima, Mexico. Geol. Soc. Lond., Spec. Publ. 213 (1), 263–280. http://dx.doi.org/10.1144/GSL.SP.2003.213.01.16.

Varley, N., Arámbula-Mendoza, R., Sanderson, R., Stevenson, J., 2010. Generation of Vulcanian activity and long-period seismicity at Volcán de Colima, Mexico. J. Volcanol. Geotherm. Res. 198 (1 - 2), 45–56. http://dx.doi.org/10.1016/j.jvolgeores.2010.08.009.

Vignaroli, G., Aldega, L., Balsamo, F., Billi, A., De Benedetti, A.A., De Filippis, L., Rossetti, F., 2014. A way to hydrothermal paroxysm, Colli Albani volcano, Italy. Geol. Soc. Am. Bull. B31139-1 http://dx.doi.org/10.1130/B31139.1.

Wallace, P., Anderson Jr., A.T., 2000. Volatiles in Magmas. In: Sigurdsson, H., Houghton, B., McNutt, S.R., Rymer, H., Stix, J. (Eds.), Encyclopedia of Volcanoes. Academic Press.

Wright, H., Cashman, K.V., Gottesfeld, E.H., Roberts, J.J., 2009. Pore structure of volcanic clasts: measurements of permeability and electrical conductivity. Earth Planet. Sci. Lett. 280 (1), 93–104. http://dx.doi.org/10.1016/j.epsl.2009.01.023.

Wright, H., Roberts, J.J., Cashman, K.V., 2006. Permeability of anisotropic tube pumice: model calculations and measurements. Geophysical research letters 33 (17). http://dx.doi.org/10.1029/2006GL027224.

Yokoyama, T., Takeuchi, S., 2009. Porosimetry of vesicular volcanic products by a water-expulsion method and the relationship of pore characteristics to permeability. J. Geophys. Res. Solid Earth (1978–2012) 114 (B2). http://dx.doi.org/10.1029/2008JB005758.

Zhu, W., Wong, T.F., 1996. Permeability reduction in a dilating rock: network modeling of damage and tortuosity. Geophys. Res. Lett. 23 (22), 3099–3102. http://dx.doi.org/10.1029/96GL03078.

Zhu, W., Baud, P., Wong, T.F., 2010. Micromechanics of cataclastic pore collapse in limestone. Journal of Geophysical Research: Solid Earth (1978–2012) 115 (B4). http://dx.doi.org/10.1029/2009JB006610.

Zhu, W., Baud, P., Vinciguerra, S., Wong, T.F., 2011. Micromechanics of brittle faulting and cataclastic flow in Alban Hills tuff. J. Geophys. Res. Solid Earth (1978–2012) 116 (B6). http://dx.doi.org/10.1029/2010JB008046.